NOTCH1 mitochondria localization during heart development promotes mitochondrial metabolism and the endothelial-to-mesenchymal transition in mice

Jie Wang[1,2,3,9], Rui Zhao[1,4,9], Sha Xu [5,9], Xiang-Yu Zhou[6], Ke Cai[1], Yu-Ling Chen[1], Ze-Yu Zhou[1], Xin Sun[1], Yan Shi[1], Feng Wang[2,3] ✉, Yong-Hao Gui[2,3] ✉, Hui Tao [7] ✉ & Jian-Yuan Zhao [1,4,8] ✉

Notch signaling activation drives an endothelial-to-mesenchymal transition (EndMT) critical for heart development, although evidence suggests that the reprogramming of endothelial cell metabolism can regulate endothelial function independent of canonical cell signaling. Herein, we investigated the crosstalk between Notch signaling and metabolic reprogramming in the EndMT process. Biochemically, we find that the NOTCH1 intracellular domain (NICD1) localizes to endothelial cell mitochondria, where it interacts with and activates the complex to enhance mitochondrial metabolism. Targeting NICD1 to mitochondria induces more EndMT compared with wild-type NICD1, and small molecule activation of PDH during pregnancy improves the phenotype in a mouse model of congenital heart defect. A *NOTCH1* mutation observed in non-syndromic tetralogy of Fallot patients decreases NICD1 mitochondrial localization and subsequent PDH activity in heart tissues. Altogether, our findings demonstrate NICD1 enrichment in mitochondria of the developing mouse heart, which induces EndMT by activating PDH and subsequently improving mitochondrial metabolism.

Mutations in the *NOTCH1* gene, which encodes the major receptor protein NOTCH1 in the Notch signaling pathway, may cause various congenital heart defects (CHDs), including bicuspid aortic valve (BAV), aortic stenosis, ventricular septal defect, hypoplastic left heart syndrome, and tetralogy of Fallot (TOF)[1,2]. *NOTCH1* is the most frequently mutated gene in non-syndromic TOF[3]. NOTCH1 intracellular domain

(NICD1), the activated form of NOTCH1, is produced via a two-step proteolytic cleavage, following membrane receptor-ligand interaction[4]. During the cardiac looping stage of cardiogenesis, as the developing heart receives progenitor cells from the second heart field and neural crest cells and forms endocardial cushions, NICD1 exists in the endocardium of the atrioventricular canal and

[1]Institute for Developmental and Regenerative Cardiovascular Medicine, Xinhua Hospital, Shanghai Jiao Tong University School of Medicine, Shanghai, China. [2]Cardiovascular Center, Children's Hospital of Fudan University, Shanghai, China. [3]National Health Commission (NHC) Key Laboratory of Neonatal Diseases (Fudan University), Children's Hospital of Fudan University, Shanghai, China. [4]MOE-Shanghai Key Laboratory of Children's Environmental Health, Xinhua Hospital, Shanghai Jiao Tong University School of Medicine, Shanghai, China. [5]State Key Laboratory of Oncology in South China, Guangdong Provincial Clinical Research Center for Cancer, Sun Yat-sen University Cancer Center, Guangzhou, P. R. China. [6]Obstetrics & Gynecology Hospital of Fudan University, Fudan University, Shanghai, China. [7]Department of Cardiothoracic Surgery, Second Hospital of Anhui Medical University, Anhui Medical University, Hefei, China. [8]International Human Phenome Institutes (Shanghai), Shanghai, China. [9]These authors contributed equally: Jie Wang, Rui Zhao, Sha Xu. ✉e-mail: fmwong@126.com; yhgui@fudan.edu.cn; taohui@ahmu.edu.cn; zhaojy@vip.163.com

periendocardial cells of the endocardial cushions, with limited detection in the myocardium, consistent with the active endothelial-to-mesenchymal transition (EndMT) process[5,6].

EndMT was initially observed in endocardial cushion formation during embryonic valvuloseptal morphogenesis, wherein endocardial/endothelial cells (ECs) detach from the endocardium, transition to mesenchymal cells, and invade the matrix between the endocardium and myocardium, leading to cushion formation[7]. Impaired EndMT may cause various CHDs related to malformed valves or misaligned septum[8], including TOF[9], atrioventricular septal defect[10], and BAV[11]. Several cytokines and signaling pathways, including interleukin-1β (IL-1β), interleukin-6, bone morphogenetic proteins (BMP), transforming growth factor β (TGF-β), vascular endothelial growth factor (VEGF), and Wnt signaling, induce or regulate EndMT[7]. However, the underlying mechanism remains elusive.

During EndMT, ECs undergo changes in morphology, cell polarity, migration, and contractile abilities[12] as well as a shift in energetic metabolism. Compared with mesenchymal cells, ECs are more dependent on glycolysis[13]. Recent studies reveal that metabolism strongly regulates EC homeostasis and is not just a response to cytokines[14,15]. Endothelial fatty acid metabolism impairment alone, by knocking down endothelial carnitine palmitoyltransferase II (*Cpt2*), induces EndMT[16], raising questions about the role of metabolism in EndMT.

Studies suggested that NOTCH1 induces EndMT in vivo and in vitro[17–19]. This is attributed to canonical Notch signaling, wherein NICD1 translocates to the nucleus and regulates the transcription of target genes such as *SLUG*, of the *SNAIL* family, and downstream vascular endothelial cadherin (*VE-cadherin*)[20,21], working synergistically with BMP and TGF-β signaling pathways[22]. However, its role in the mitochondria remains unknown. Interestingly, besides its canonical role in cell fate determination[23], Notch signaling conveys environmental metabolic cues, such as plasma glucose levels[24] and inflammatory lipids[25], to regulate intracellular nutrient metabolism and reprogram cellular energetic metabolism[26,27]. Recent studies also indicate the mitochondrial localization of NICD1 in M1 macrophages[26] and triple-negative breast cancer cells[28]. Moreover, enhanced CHD phenotype is observed in *Notch1*-mutated murine models born to diabetic mothers[29], indicating the involvement of NOTCH1 in regulating metabolism, which may contribute to the induction of EndMT and CHD pathogenesis.

Herein, the study objective is to investigate the role of NICD1 in the mitochondria of developing mouse fetal hearts and its induction of EndMT through the activation of PDH and mitochondrial metabolism.

Results

NICD1 is enriched in mouse cardiac EC and cell line mitochondria

Nuclear translocation has long been considered the major intracellular distribution pattern of NICD1, but recent studies indicate the mitochondrial localization of NICD1 in M1 macrophages[26] and triple-negative breast cancer cells[28]. To investigate the intracellular distribution pattern of NICD1 in cardiac ECs, we harvested newborn SD rat hearts and isolated ECs by recognizing cell marker CD31 through flow cytometry. Following extraction of subcellular fraction via differential centrifugation, we detected NICD1 in the mitochondria of cardiac ECs (Fig. 1A). Regarding whether mitochondrial localization of NICD was tissue-specific or stage-specific during embryo heart development, we detected NICD1 in the mitochondria of cardiomyocytes and cardiac ECs isolated from fetal mouse heart tissues collected at E11.5, when the separation of the outflow tract, atria, and ventricles is initiated, and at E14.5, when the separation is completed and valves are established[30]. NICD1 detection was especially prominent in mitochondria of cardiac ECs at E11.5 (Fig. 1B).

We further detected NICD1 in the subcellular mitochondrial fractions of HUVEC and HEK293T cell lines (Fig. 1C). Furthermore, we detected NICD1 in the mitochondria of several tumor cell lines with high NOTCH1 expression, such as the human gastric cancer cell line MKN45 and pancreatic cancer cell line BxPC-3 (Fig. 1C). These findings suggest that NICD1's mitochondrial localization may be prevalent in actively developing and rapidly proliferating cells. Moreover, immunofluorescence staining of NOTCH1, utilizing MitoTracker Red CMXRos as a mitochondria marker, revealed the colocalization of NICD1 and mitochondria in HUVEC and HEK293T cells (yellow dots in Fig. 1D, E), confirming mitochondrial enrichment of NICD1.

To understand the mechanism of NICD1 mitochondrial translocation, we first adopted the online Deepmito bioinformatic tool (http://busca.biocomp.unibo.it/deepmito/)[31], and the prediction revealed that NICD1 may be located in mitochondrial matrix (Supplementary Fig. 1A). Most mitochondrial matrix proteins are synthesized in the cytosol and have characteristic amino-terminal presequences that form positively-charged amphipathic α-helix[32]. Using online bioinformatics tools, including iPSORT (http://ipsort.hgc.jp), TargetP-2.0 (http://www.cbs.dtu.dk/services/TargetP/)[33], and MitoFate (http://mitf.cbrc.jp/MitoFates/cgi-bin/top.cgi) (Supplementary Fig. 1B–D)[34], we found no known presequences, suggesting the adoption of internal signals, typically composed of a stretch of continuous hydrophobic amino acids, during NICD1's translocation[32,35]. Accordingly, we identified eight stretches (M1-M8) (Fig. 1F) of continuous hydrophobic amino acids[35,36], among which deletion of M4 (G2126-L2135, GAPLGGTPTL), M5 (A2256-G2262, AALGGGG), and M6 (V2330-L2335, VAPGPL) significantly reduced the mitochondrial localization of exogenously expressed NICD1 in both HUVEC and HEK293T cells (Fig. 1G). These findings suggest that NICD1 translocates to the mitochondrial matrix via its internal signals.

NICD1 interacts with the main subunit of mitochondrial metabolic enzyme PDH

NICD1 regulates gene transcription in nucleus, but its function in mitochondria is unknown. To investigate the potential function of NICD1 in mitochondria, we identified NICD1 interacting proteins. Mass spectrometry indicated 427 proteins might interact with NICD1 (Supplementary Fig. 2A and Supplementary Data 1). Gene-ontology analysis revealed that NICD1-interacting proteins were enriched in mitochondrial functions and metabolic pathways, including the tricarboxylic acid (TCA) cycle (Supplementary Fig. 2C). Three metabolic enzymes in the mitochondrial matrix were found to interact with NICD1, namely isocitrate dehydrogenase 3B (IDH3B), citrate synthase (CS), and PDHB (Supplementary Fig. 2B). CO-IP assays performed in HEK293T cells confirmed the interaction of exogenous NICD1 with PDHB (Fig. 2A), but not with CS or IDH3B (Supplementary Fig. 3A). Subsequently, through endogenous CO-IP, we confirmed the interaction between endogenous NICD1 and PDHB in primary rat cardiac ECs (Fig. 2B) and mouse cardiac ECs (Supplementary Fig. 3B). Moreover, we confirmed the interaction by identifying the binding region in NICD1. Truncated NICD1 was tested for its ability to interact with PDHB, which revealed that the removal of residuals from the N-terminus to the second nuclear localization sequence region led to loss of binding ability of NICD1 to PDHB (Fig. 2C).

In the bimolecular fluorescence complementation (BiFC) assay, a fluorescent signal occurs when two non-fluorescent fragments are brought together by two interacting proteins. To eliminate the uneven molecular weight effect, we fused our target proteins to either the C- or N-terminus of Venus and harvested VN-PDHB, VC-PDHB, VN-NICD1, and VC-NICD1. VN-bJun and VC-bFos were constructed as the positive control (Fig. 2D). Upon co-transfection of VN-PDHB and VC-NICD1 (reaction 1, Fig. 2E) or VN-NICD1 and VC-PDHB (reaction 2, Fig. 2F)
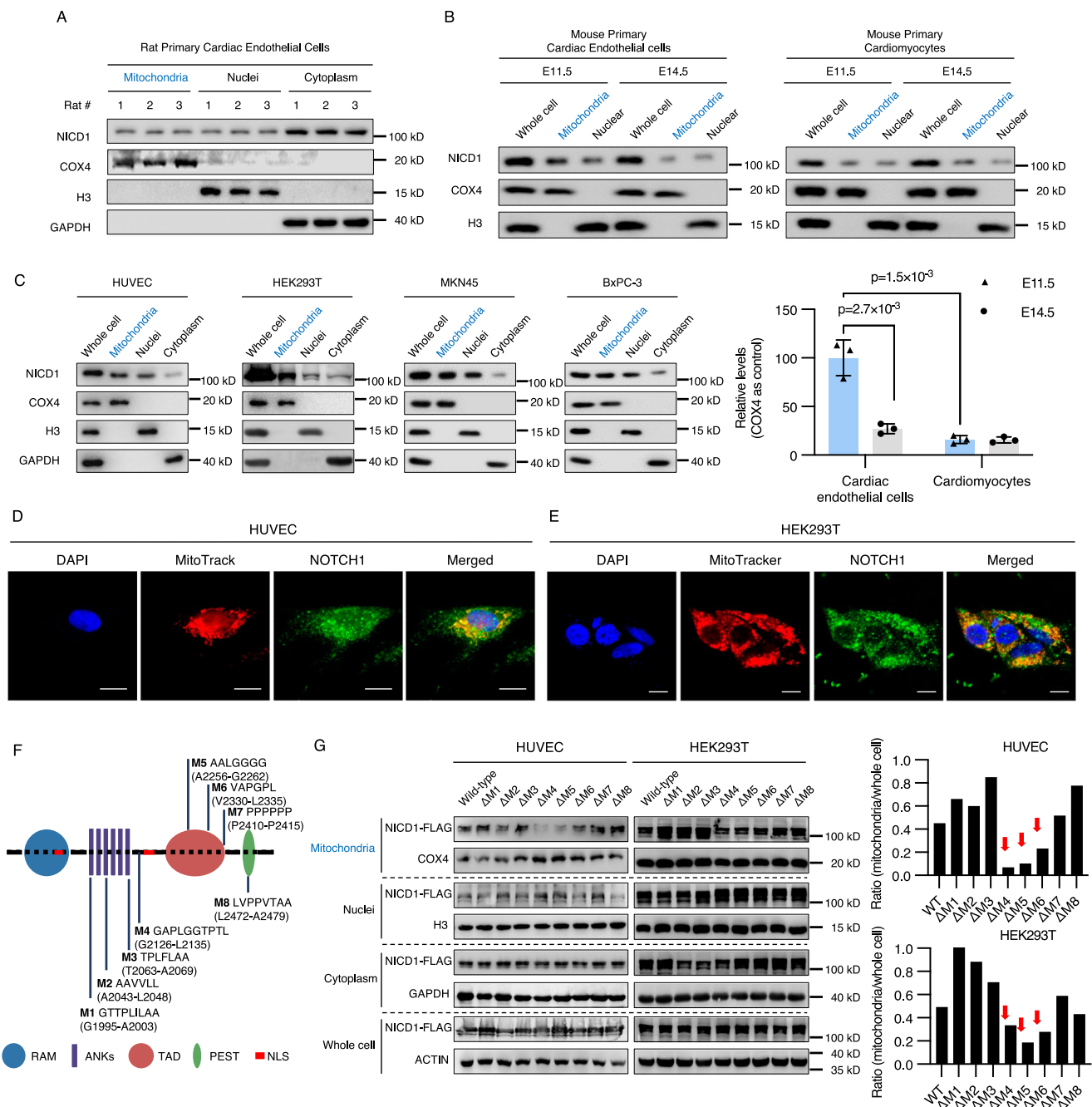
Fig. 1 | Intracellular distribution pattern of NOTCH1 intracellular domain (NICD1) in mouse cardiac endothelial cells and cultured cell lines.
A Representative western blot illustrating NICD1 levels in subcellular fractions from rat primary cardiac endothelial cells. Mitochondrial (Cytochrome C oxidase subunit 4, COX 4), nuclear (Histone H3, H3), and cytoplasmic (glyceraldehyde-3-phosphate dehydrogenase, GAPDH) markers were used. Three experiments were repeated independently with similar results. **B** Top: representative western blot illustrating NICD1 levels in whole-cell lysates and subcellular fractions from mouse primary cardiac endothelial cells and cardiomyocytes from mouse embryo hearts at E11.5 and E14.5. Bottom: Relative levels of mitochondrial NICD1 in mouse primary cardiac endothelial cells and cardiomyocytes ($n = 3$). Data are presented as mean values ± SD. *P* values were calculated by unpaired Student's *t* test with two-tailed analysis without adjustments. **C** Representative western blot illustrating NICD1 levels in cultured human umbilical vein endothelial cell (HUVEC), human embryonic

kidney 293 cells (HEK293T), MKN45 gastric cancer cells, and BxPC-3 pancreatic cancer cells. Three experiments were repeated independently with similar results. **D**, **E** Immunofluorescence confocal microscopy images showing the colocalization of NOTCH1 (green) and mitochondria (red) in HUVEC and HEK293T cells. Results are representative of three different experiments. Scale bars: 20 μm for HUVEC and 10 μm for HEK293T. **F** Location and sequences of putative internal signals (M1–8) in NICD1. RAM Rbp-associated molecule domain, ANKs ankyrin repeats, TAD transcription activation domain, PEST proline (P), glutamic acid (E), serine (S), threonine (T) degradation domain, NLS nuclear localization signals. **G** Left: representative western blot of NICD1 levels in subcellular fractions from HUVEC and HEK293T cells overexpressing FLAG-tagged wild-type NICD1 or internal signal-deleted NICD1 (ΔM1–8). Three experiments were repeated independently with similar results. Right: Ratio of NICD1 level in mitochondria to whole-cell lysate in HUVEC and HEK293T cells. Source data are provided as a Source Data file.
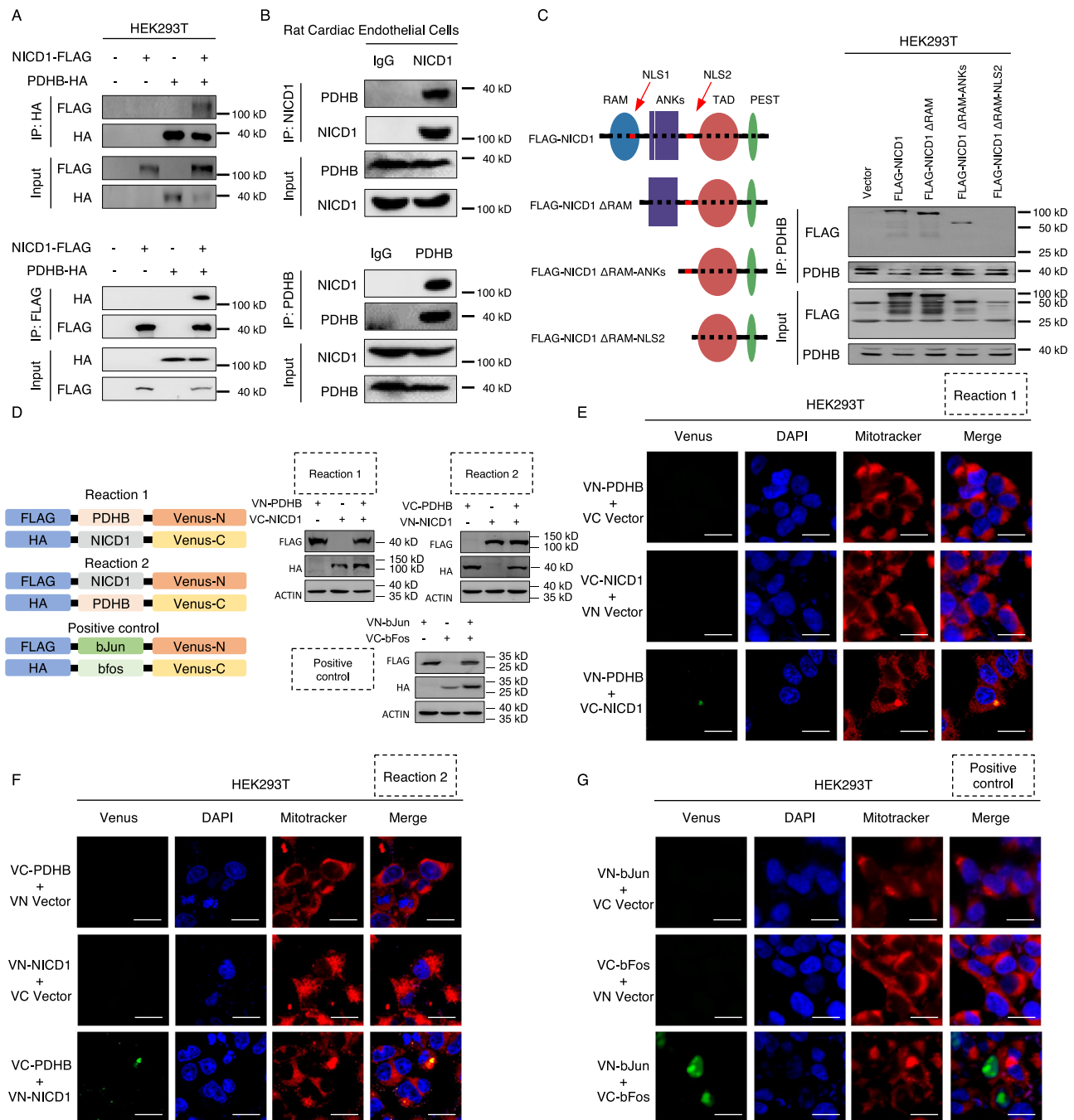
Fig. 2 | Interaction between NOTCH1 intracellular domain (NICD1) and mitochondrial pyruvate dehydrogenase E1 subunit beta (PDHB).
**A** Co-immunoprecipitation (CO-IP) of exogenous NICD1 and PDHB in human embryonic kidney 293T (HEK293T) cells. **B**, CO-IP of endogenous NICD1 and PDHB in rat cardiac endothelial cells. **C** Left: Schematic of truncated NICD1. RAM, Rbp-associated molecule domain; ANKs, ankyrin repeats; TAD, transcription activation domain; PEST, proline (P), glutamic acid (E), serine (S), threonine (T) degradation domain; NLS, nuclear localization signals. Right: CO-IP of exogeneous truncated NICD1 and PDHB in HEK293T cells. **D** Left: Schematic of recombinant proteins constructed for bimolecular fluorescence complementation (BiFC) assays: PDHB fused with N-terminus of Venus (VN-PDHB) and NICD1 fused with C-terminus of

Venus (VC-NICD1) in reaction 1, NICD1 fused with VN (VN-NICD1) and PDHB fused with VC (VC-PDHB) in reaction 2, and bJun (the binding domain of Jun [the 257–318 amino acids]) fused with VN (VN-bJun) and bFos (the binding domain of Fos [the 118–210 amino acids]) fused with VC (VC-bFos) in positive control. Right: Representative western blot illustrating the expression level of recombinant proteins in HEK293T cells. **E–G** BiFC assay exhibiting the interactions of VN-PDHB and VC-NICD1 in reaction 1(**E**), VC-PDHB and VN-NICD1 in reaction 2 (**F**), and VN-bJun and VC-bFos in positive control (**G**) in green dots and their intracellular distribution (Scale bar = 20 µm). Three experiments were repeated independently with similar results for **A–G**. Source data are provided as a Source Data file.

expression vectors into HEK293T cells, fluorescent signals were observed outside the nucleus, in contrast to nuclear-fluorescent signals resulting from bJun and bFos complementation (positive control, Fig. 2G). These results indicated that NICD1 interacts with PDHB in the mitochondria.

Mitochondrial NICD1 activates PDH and mitochondrial respiration
To evaluate the effect of the above protein-protein interaction, we initially examined the expression levels of PDHB, CS, and IDH3B in HEK293T cells upon NICD1 overexpression or *NOTCH1* knockdown and

Figure 3
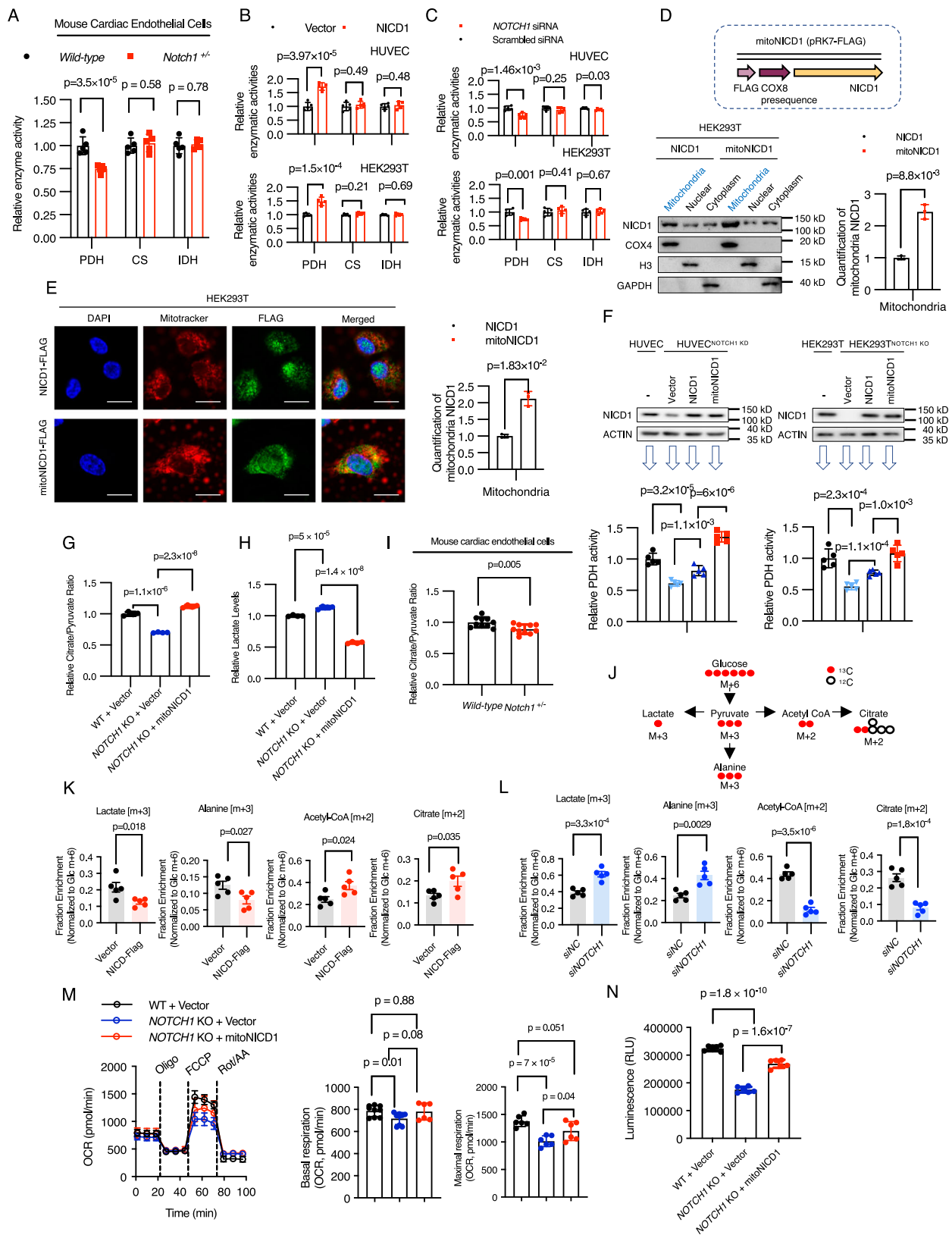
found no significant alterations (Supplementary Fig. 4). Subsequently, we measured the enzymatic activity of PDH, CS, and IDH in isolated mouse cardiac ECs from wild-type or *Notch1*^{+/−} mouse, revealing an obvious decrease in PDH activity in *Notch1*^{+/−} mouse (Fig. 3A). Similarly, PDH activity increased in vitro in cell lines overexpressing exogenous NICD1 (Fig. 3B) and decreased in *NOTCH1* knockdown cells (Fig. 3C),

while CS and IDH activity levels remained unchanged in HUVEC and HEK293T cells. These results suggest that the interaction between NICD1 and PDHB may be significant.

To further confirm the mitochondrial effect of NICD1, we constructed a plasmid expressing recombinant mitochondria-targeted NICD1 (mitoNICD1), containing a 23-amino acid COX8 presequence

Fig. 3 | Mitochondria-located NOTCH1 intracellular domain (NICD1) activation of pyruvate dehydrogenase (PDH) and mitochondrial respiration. A Enzymatic activity of PDH, CS, and IDH in mouse cardiac ECs isolated from mice (*n* = 5). **B** Enzymatic activity of PDH, CS, and IDH in cells (*n* = 5). **C** Enzymatic activity of PDH, CS, and IDH in cells transfected with siNC or *NOTCH1* siRNA (si*NOTCH1*) (*n* = 5). **D** Top: schematic of recombinant mitoNICD1 protein containing a pre-sequence of cytochrome oxidase subunit 8 (COX8). Bottom: representative western blot illustrating intracellular distribution of wild-type NICD1 and mitoNICD1 (left) and quantification of mitochondrial NICD1 (*n* = 3) (right). **E** Representative immunofluorescence confocal microscopy illustrating intracellular distribution of NICD1 and mitoNICD1 (left) and the quantification of mitochondrial NICD1 (*n* = 3) (right) (Scale bar = 20 μm). **F** Representative western blot illustrating NICD1 levels (Top) and PDH activities (Bottom) in cells with different treatments (*n* = 5). **G** Relative ratio of citrate to pyruvate in wild-type (WT) cells, *NOTCH1* KO cells and *NOTCH1* KO cells expressing mitoNICD1 (*n* = 4). **H** Relative lactate level in WT cells, *NOTCH1* KO cells and *NOTCH1* KO cells expressing mitoNICD1 (*n* = 4). **I** Relative

ratio of citrate to pyruvate in mouse cardiac endothelial cells isolated from wild-type and *Notch1*$^{+/-}$ mice (*n* = 10). **J** Schematic of possible fates for [U-^{13}C]glucose. **K** Fraction enrichment of lactate [m+3], alanine [m+3], acetyl-CoA [m+2], and citrate [m+2] in cells expressing exogenous wild-type NICD1 or not (*n* = 5). **L** Fraction enrichment of lactate [m+3], alanine [m+3], acetyl-CoA [m+2], and citrate [m+2] in cells transfected with scramble siNC or si*NOTCH1* (*n* = 5). **M** Left: profile of oxygen consumption rate (OCR) of WT cells, *NOTCH1* KO cells, and *NOTCH1* KO cells expressing mitoNICD1. Oligomycin (Oligo), 2-[2-[4-(trifluoromethoxy)phenyl]hydrazinylidene]-propanedinitrile (FCCP), antimycin and rotenone (Rot/AA) were supplemented at 20, 50, and 80 min during the test. Right: Quantification of basal respiration (*n* = 9) and maximal respiration indicated by OCR (*n* = 6). **N** ATP levels of WT cells, *NOTCH1* KO cells, and *NOTCH1* KO cells expressing mitoNICD1 as indicated by luminescence (*n* = 6). Source data are provided as a Source Data file. For **A**–**I** and **K**–**N**, data are presented as mean values ± SD; *P* values were calculated by unpaired Student's t-test with two-tailed analysis without adjustments.

and an N-terminal FLAG-tag (Fig. 3D). Increased enrichment of mito-NICD1 in mitochondria was confirmed compared to NICD1 (Fig. 3D, E). Next, we knocked down *NOTCH1* in HUVEC (HUVEC$^{NOTCH1\ KD}$) and knocked out *NOTCH1* in HEK293T (HEK293T$^{NOTCH1 KO}$) to nullify the effect of endogenous NICD1 and measured PDH activity levels in these cells expressing exogenous NICD1, mitoNICD1, or none. We confirmed decreased PDH activity in NOTCH1-deficient cells compared with wild-type cells, with both exogenous NICD1 and mitoNICD1 partially rescuing PDH activity, although mitoNICD1 had a better effect in restoring PDH activity (Fig. 3F). These results indicated that while NICD1 may activate PDH by entering the nucleus and activating the transcription of pyruvate dehydrogenase phosphatase 1 (PDP1)[26], mitochondrial NICD1 may directly activate PDH by binding PDHB, independent of transcriptional regulation.

Two copies of PDHB and PDHA form one α2β2 heterotetrametric PDH[37], which catalyzes the conversion of pyruvate into acetyl coenzyme A (acetyl-CoA) and plays a gating role in controlling the ratio of glucose catabolism into TCA cycle or lactate production[38,39]. To investigate NOTCH1-induced metabolite changes, we analyzed HEK293T cells and observed a significant reduction in the citric acid/pyruvate ratio upon *NOTCH1* knockout, an effect rescued by exogenous mitoNICD1 expression (Fig. 3G). The relative lactate level increased upon *NOTCH1* knockout, which was reversed by mitoNICD1 overexpression in HEK293T cells (Fig. 3H). We also detected a significantly decreased citric acid/pyruvate ratio in cardiac ECs isolated from *Notch1*$^{+/-}$ mouse embryos at E14.5 compared with wild-type (Fig. 3I). To further confirm metabolite alterations, glucose metabolism tracing using [U-^{13}C] glucose (Fig. 3J) revealed increased TCA cycle flux in HUVEC cells overexpressing NICD1, indicated by increased levels of acetyl-CoA and citrate and decreased levels of lactate and alanine (Fig. 3K), and decreased TCA cycle flux in *NOTCH1* knockdown HUVEC cells, indicated by decreased acetyl-CoA and citrate levels and increased lactate and alanine levels (Fig. 3L).

The accelerated TCA cycle is always correlated with enhanced oxidative phosphorylation (OXPHOS) and ATP synthesis[40]. Assessment of oxygen consumption rate in HEK293T cells using Seahorse Mito Stress assays revealed reduced basal and maximal respiration levels in *NOTCH1* KO cells, which were rescued by exogenous mitoNICD1 expression (Fig. 3M), indicating that mitoNICD1-stimulates mitochondrial respiration and increases cellular respiration capacity. Furthermore, quantification of total ATP levels revealed a significant decrease upon *NOTCH1* knockout, partially restored by the exogenous expression of mitoNICD1 in HEK293T cells (Fig. 3N). These results show that mitochondrial NICD1 accelerates the TCA cycle and enhances oxygen consumption and ATP synthesis.

Mitochondrial NICD1 Activates PDH by Dephosphorylating PDHA1

The PDC consists of three core enzymatic components, including PDH, DLAT, and DLD[41], which are present majorly in mitochondria and also found in nucleus[42]. The intracellular distribution of each component may affect the complex activity. In *NOTCH1*-KO and control HEK293T cells, we assessed PDHA1, PDHB, DLAT, and DLD levels in subcellular fractions and observed no changes in the intracellular distribution of PDC components upon *NOTCH1* knockout (Fig. 4A). We had established the interaction between NICD1 and PDHB (Fig. 3). So, here we performed endogenous CO-IP of NICD1 and detected PDHA1, DLAT, and DLD in the precipitates, both in HUVEC and HEK293T cells (Fig. 4B). However, GST pull-down assays revealed that NICD1 only bound to PDHB (Fig. 4C), indicating that NICD1 binds to PDC through direct interaction with PDHB.

Efficient catalysis of pyruvate to acetyl-CoA by PDH depends on the integrity of the PDC structure, comprising PDH, DLAT, and DLD, which allows quick movement of reaction intermediates. Compared each PDC component level with endogenous immunoprecipitation, we observed no significant difference in HEK293T$^{NOTCH1 KO}$ cells or those expressing exogenous NICD1 or mitoNICD1, suggesting that whole-cell and mitochondrial NICD1 expression levels do not affect PDC integrity (Fig. 4D). Moreover, mito-NICD1 overexpression did not alter mRNA levels of PDC subunits in HEK293T cells (Supplementary Fig. 5).

PDKs and PDPs, regulatory parts of PDC, respectively inhibit PDH activity by phosphorylating PDHA1 on ser293, ser300, and ser232, and activate PDH by dephosphorylating PDHA1[43]. Overexpression of NICD1 or mitoNICD1 significantly reduced PDHA1 phosphorylation at ser293, ser300, and ser232, particularly mitoNICD1, in both HUVEC and HEK293T cells (Fig. 4E). Conversely, *NOTCH1* knockdown in HUVEC or *NOTCH1* knockout in HEK293T cells significantly increased PDHA1 phosphorylation compared with control (Fig. 4F). Assessing whether NICD1 impedes the contact between PDHA1 and regulatory PDKs and PDPs under NICD1 or mitoNICD1 overexpression conditions revealed that mitoNICD1 overexpression significantly decreased the interaction between PDHA1 and PDK1-4 and PDP1 in both HUVEC and HEK293T cells (Fig. 4G). Moreover, we found increased interaction between PDHA1 and PDK1 or PDP1 in cardiac ECs of *Notch1*$^{+/-}$ mice compared to wild-type mice (Fig. 4H), along with increased PDHA1 phosphorylation (Fig. 4I). These results from *Notch1*$^{+/-}$ mice verified the findings in HEK293T cells and indicated that NOTCH1 deficiency leads to PDH inactivation through increased PDHA1 phosphorylation.

MitoNICD1-induced PDH activation promotes EndMT

Exogenous NICD1 expression can induce EndMT[17]. To investigate whether this effect can be attributed to the regulation of mitochondrial metabolism by NICD1, we transfected HUVEC cells with
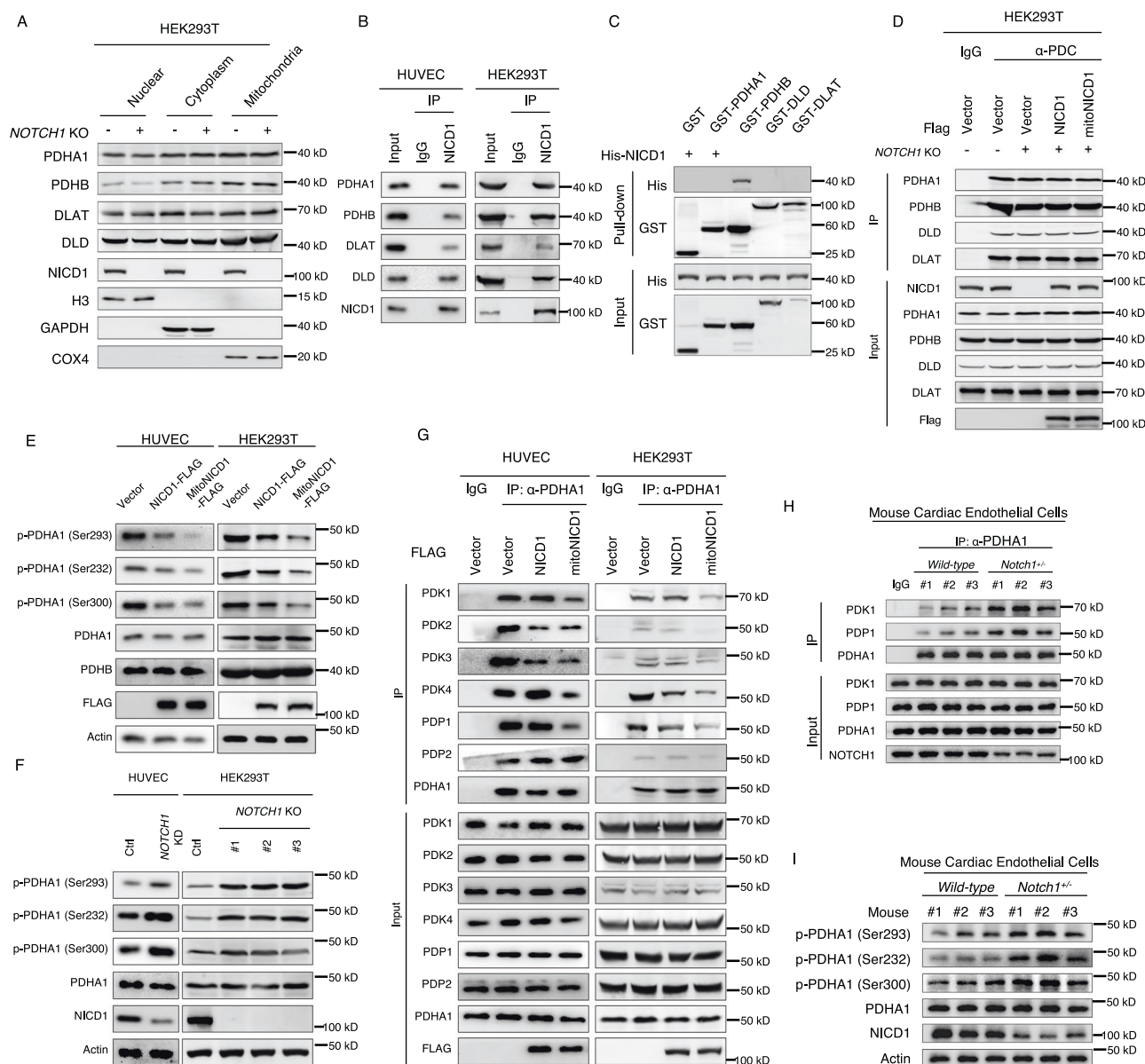
Fig. 4 | NOTCH1 intracellular domain (NICD1) impedes the binding of pyruvate dehydrogenase kinases (PDKs) to pyruvate dehydrogenase E1 subunit alpha 1 (PDHA1) and decreases the phosphorylation of PDHA1 (p-PDHA1).
A Representative western blot illustrating the intracellular distribution of pyruvate dehydrogenase complex (PDC) components in wild-type and *NOTCH1* knockout (*NOTCH1* KO) human embryonic kidney 293T (HEK293T) cells. PDHB pyruvate dehydrogenase E1 subunit beta, DLAT dihydrolipoamide S-acetyltransferase; DLD dihydrolipoyl transacetylase. **B** Endogenous co-immunoprecipitation (CO-IP) of NICD1 with PDC components in human umbilical vein endothelial cells (HUVEC) and HEK293T cells. **C** GST pull-down assay to determine in vitro binding of NICD1 to PDHA1, PDHB, DLD, and DLAT. **D** Representative western blot illustrating the level of each PDC component collected by endogenous immune-precipitation (IP) from wild-type HEK293T cells, *NOTCH1* KO HEK293T cells, *NOTCH1* KO HEK293T cells expressing exogenous NICD1, or recombinant mitochondria-targeted NICD1 (mitoNICD1). **E** Representative western blot illustrating the level of p-PDHA1 at serine 293 (Ser293), serine 232 (Ser232), and serine 300 (Ser300) in HUVEC cells

expressing NICD1 or mitoNICD1 (left) and in HEK293T cells expressing NICD1 or mitoNICD1 (right). **F** Representative western blot illustrating the level of p-PDHA1 at Ser293, Ser232, and Ser300 in wild type and *NOTCH1* knockdown (*NOTCH1* KD) HUVEC cells (left), and wild-type and *NOTCH1* KO HEK293T cells (right). **G** Representative western blot illustrating the affinity of PDKs, including PDK1, PDK2, PDK3, and PDK4, and pyruvate dehydrogenase phosphatases (PDPs), including PDP1 and PDP2, to endogenous PDHA1 collected by endogenous IP from HUVEC cells expressing NICD1, mitoNICD1 or not (left), and HEK293T cells expressing NICD1, mitoNICD1, or not (right). **H** Representative western blot illustrating the affinity of PDK1 and PDP1 to endogenous PDHA1 collected by endogenous IP from wild-type mice and *Notch1* heterozygous knockout (*Notch1*^{+/−}) mice. **I** Representative western blot illustrating the p-PDHA1 level at Ser293, Ser232, and Ser300 in mouse cardiac endothelial cells isolated from wild-type and *Notch1*^{+/−} mice. Three experiments were repeated independently with similar results for **A**–**I**. Source data are provided as a Source Data file Source data are provided as a Source Data file.

mitoNICD1 or wild-type NICD1-expression plasmids and used a combination of TGF-β1 and IL-1β as a positive control treatment as described previously[16,44]. Immunofluorescent results at 7 days post-treatment showed that cells treated with TGF-β1 and IL-1β were significantly larger than control ECs and exhibited a higher expression level of mesenchymal marker α-SMA, with

almost no expression of endothelial marker CD31 in low-power field. In high-power field, α-SMA in TGF-β1- and IL-1β-treated cells appeared in a fiber-like form, consistent with the migrating ability of mesenchymal cells. These large α-SMA-positive cells were defined as mesenchymal cells in our results (Fig. 5A).
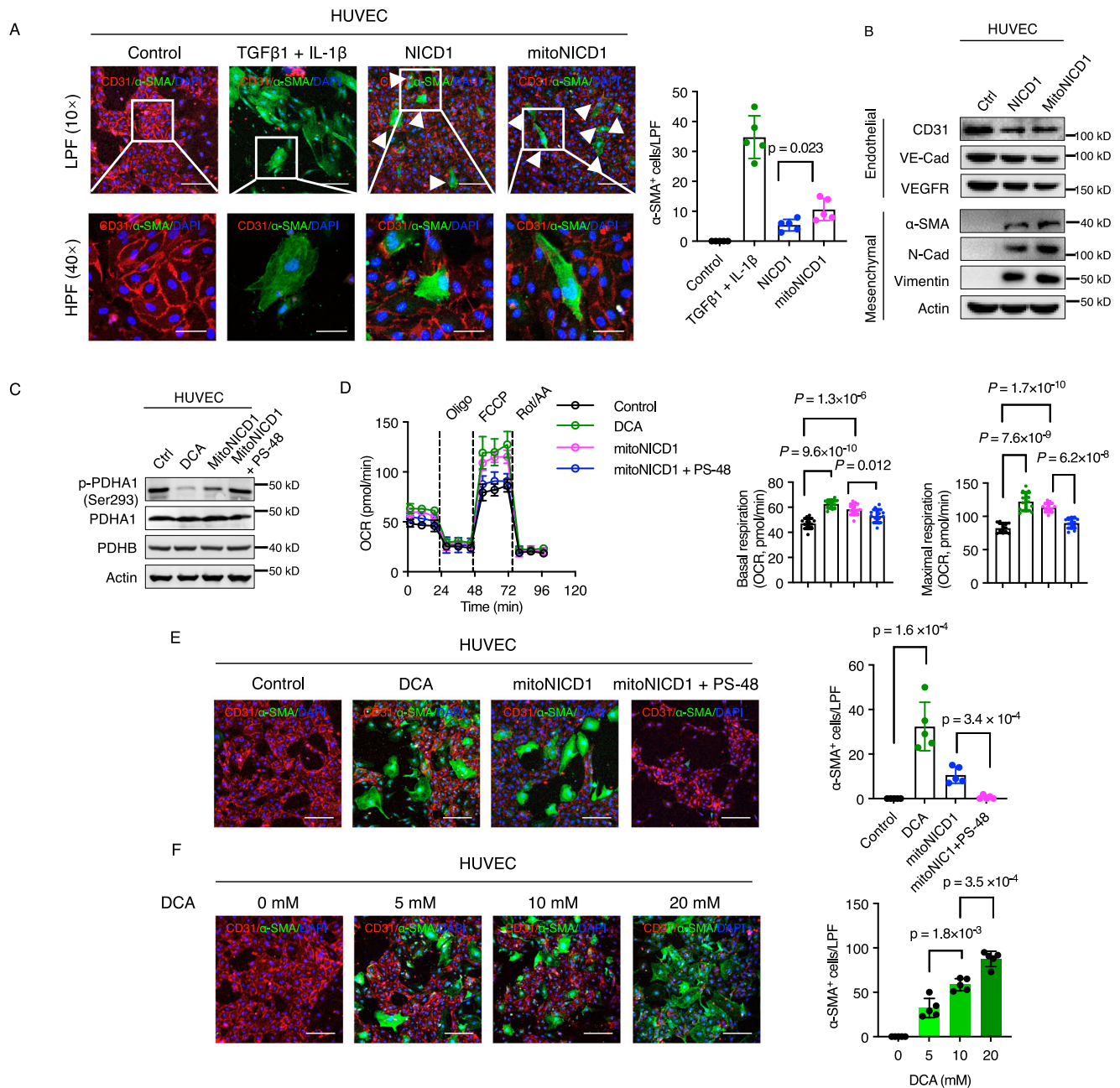
Fig. 5 | Mitochondria-targeted NOTCH1 intracellular domain (mitoNICD1)-induced pyruvate dehydrogenase (PDH) activation promotes endothelial-to-mesenchymal transition. A Left: representative immunofluorescence confocal microscopy showing the endothelial cell marker CD31 (red) and the mesenchymal cell marker α smooth muscle actin (α-SMA) (green) in human umbilical vein endothelial cells (HUVEC) treated with cytokines (10 mg/μL transforming growth factor β [TGF-β1] and 1 ng/μL interleukin-1β [IL-1β]), expressing exogenous NOTCH1 intracellular domain (NICD1), or mitoNICD1 in low-power field (LPF) (10×) (top, scale bar=200 μm) and high-power field (HPF) (×40) (bottom, scale bar = 50 μm)). Nuclei are stained with DAPI (blue). Right: Quantification of α-SMA positive (α-SMA+) cells per LPF (*n* = 5 biological samples per group). **B** Representative western blot illustrating endothelial cell markers, including CD31, vascular endothelial cadherin (VE-Cad), and vascular endothelial growth factor receptor (VEGFR), and mesenchymal cell markers, including α-SMA, N-Cadherin (N-Cad), Vimentin, and Actin, in HUVEC expressing exogenous NICD1, mitoNICD1, or not. **C** Representative western blot illustrating the phosphorylation of pyruvate dehydrogenase E1 subunit alpha 1 (PDHA1) (p-PDHA1) at serine 293 (Ser293) in HUVEC treated with

PDH-activator dichloroacetate (DCA) (10 mmol/L), expressing mitoNICD1, or expressing mitoNICD1 and supplemented with PDH inhibitor PS-48 (100 μmol/L) as well. **D** Top: profile of oxygen consumption rate (OCR) of HUVEC treated with DCA (10 mmol/L), expressing mitoNICD1, or expressing mitoNICD1 and supplemented with PS-48 (100 μmol/L) as well. Bottom: Quantification of basal respiration and maximal respiration indicated by OCR (*n* = 3 biological samples per group). **E** Left: representative immunofluorescence confocal microscopy showing CD31 (red) and α-SMA (green) in HUVEC treated with DCA (10 mmol/L), expressing mitoNICD1, or expressing mitoNICD1 and supplemented with PS-48 (100 μmol/L) as well (Scale bar=200 μm). Right: quantification of α-SMA+ cells per LPF (*n* = 5 biological samples per group). **F** Representative immunofluorescence confocal microscopy of CD31 (red) and α-SMA (green) in HUVEC treated with 5, 10, or 20 mmol/L DCA (Scale bar = 200 μm). Right: quantification of α-SMA+ cells per LPF (*n* = 5 biological samples per group). Source data are provided as a Source Data file. For **A**, **D**−**F**, data are presented as mean values ± SD; *P* values were calculated by unpaired Student's *t* test with two-tailed analysis without adjustments.

Herein, we found endothelial-derived mesenchymal cells in a background of CD31-positive ECs (Fig. 5A) in both NICD1- and mitoNICD1-expressing groups. Cell lysates from NICD1- and mitoNICD1-expressing HUVEC cells showed increased expression of mesenchymal proteins and decreased levels of endothelial markers (Fig. 5B). To confirm whether mitoNICD1 also activates PDH and enhances OXPHOS in ECs, we collected HUVEC cells 2 days after transfection and observed significantly decreased phosphorylation of the PDHA1 S293 site (Fig. 5C) and enhanced mitochondrial respiration in mitoNICD1-overexpressed HUVEC cells (Fig. 5D).

Given our findings that mitoNICD1-induced EndMT and activated PDH in HUVEC cells, we supposed that PDH activation contributes to EndMT. To test this, we adopted PS-48, a selective PDK activator, to inhibit PDH activation, and adopted DCA, a selective PDH activator, to mimic the metabolic effect of mito-NICD1 in HUVEC cells (Fig. 5C, D). Immunofluorescent results revealed that PS-48 treatment significantly reduced the number of endothelial-derived mesenchymal cells in mitoNICD1-transfected cells 7 days post-treatment, while DCA treatment alone induced substantial EndMT (Fig. 5E). Further, DCA induces EndMT in a dose-dependent manner (Fig. 5F). These results suggest that mitoNICD1-induced EndMT through PDH activation, which was blocked by PS-48 and mimicked by DCA.

MitoNICD1 Deficiency-Induced PDC Inactivation Contributes to CHD

We investigated whether NICD1-mediated PDH activation contributes to CHD risk in $Notch1^{+/-}$ C57BL/6 J mouse model. Histological analysis of cardiac phenotypes of embryos of 8-week-old $Notch1^{+/-}$ male mice and 8-week-old wild-type female mice at E14.5 revealed that CHD incidence in $Notch1^{+/-}$ embryos did not increase compared with that in wild-type embryos. However, exposure of pregnant mice to environmental stress, such as low-dose Hcy, significantly increased CHD incidence in $Notch1^{+/-}$ embryos, while the wild-type offspring remained unaffected (Figs. 6A and S6). This result suggested that $Notch1^{+/-}$ mice exhibit no cardiac phenotypes, but had higher CHD risk under stress compared to wild-type mice. PDH activity in E12.5 mouse heart tissue was significantly lower in $Notch1^{+/-}$ mice than in wild-type mice (Fig. 6B). Furthermore, DCA intervention in pregnant mice enhanced PDH activity in fetal hearts (Fig. 6B) and decreased CHD incidence in $Notch1^{+/-}$ offspring compared with the control group (Fig. 6A). These results suggested that NICD1 deficiency decreases PDH activity and increases CHD risk. PDH activation can rescue the teratogenic effect caused by NICD1 deficiency.

In 300 TOF patients, we identified 15 $NOTCH1$ missense mutations through Sanger DNA Sequencing, with five located in the NICD1 region (Figs. 6C and S7). We constructed NICD1 mutants for these five mutations and found that the R2263Q mutation hindered NICD1 entry into the mitochondria of HUVEC cells (Fig. 6D). We found that the M5 segment (aa.2256-2262) within NICD1 is crucial for NICD1 entry into the mitochondria (Fig. 1G). The R2263Q mutation discovered here is adjacent to the M5 segment, further confirming the importance of this region in NICD1 mitochondrial entry. Consequently, the NICD1 R2263Q mutant exhibited decreased binding ability with PDHB (Fig. 6E). Next, in HEK293T$^{NOTCH1-KO}$ and HUVEC$^{NOTCH1-KD}$ cells, the NICD1 R2263Q mutant failed to inhibit PDHA1 phosphorylation similar to the wild-type or other NICD1 mutants (Fig. 6F), thereby inefficiently activating PDH (Fig. 6G).
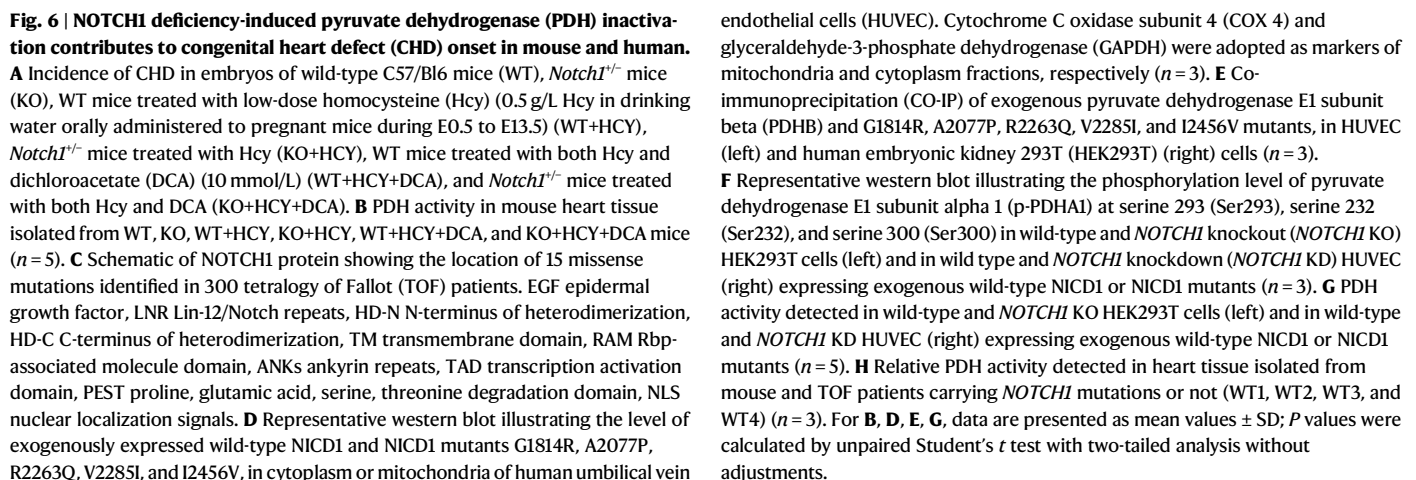
Consistent with this, heart tissue samples from carriers of these gene mutations exhibited lower PDH activity, particularly in carriers of the R2263Q (c.6788G>A) mutation, than those from patients with other $NOTCH1$ mutations or without $NOTCH1$ mutations (Fig. 6H). These clinical findings confirm the role of NICD1 in PDH activity regulation via its interaction with PDHB.

Discussion

This study found that NICD1 is enriched in the mitochondria of developing mouse fetal hearts and PDH activation contributes to NICD1-induced EndMT. $NOTCH1$ mutations in TOF patients impair mitochondrial translocation, thus lowering PDH activity.

Notch signaling, initially identified through the observation of notched wings in mutant fruit flies 100 years ago, is considered to control cell lineage determination, immune system activation, and organ and tissue development[45]. Recent studies have suggested its involvement in rewiring cell metabolism[46], thus influencing cell fate decision[26], but multiple reports considered the metabolic outcomes to be context-dependent and elusive[47], with the underlying mechanism not fully elucidated yet. Several pathways, including HIF-1α[48], PI3K/AKT[49], NF-κB[50,51], and mTORC[52] pathways, have been considered. A recent study reported NICD1 enrichment at the CSL site in the promoter of $Pdp1$ and that it can activate PDH by transcriptionally activating PDP1, thus decreasing PDHA1 phosphorylation. In our study, we observed that mitochondrial NICD1 directly interacted with PDHB in the mitochondria matrix, hampering the access of PDK1-4 and PDP1 to PDHA1 and thereby decreasing PDHA1 phosphorylation and activating PDH. Further structural studies are warranted to prove and visualize this process.

Since the initial report on $NOTCH1$ mutations in two families with BAV in 2005[2], a growing number of $NOTCH1$ mutations are considered pathogenetic to CHDs, with $NOTCH1$ being the most frequently mutated gene in non-syndromic TOF[3]. In this study, we identified 15 NOTCH1 missense mutations in 300 TOF patients, 5 of which located in NICD domain, and found that the c.6788G>A (a.R2263Q) mutation hindered NICD1 entry into the mitochondria and exhibited decreased binding ability with PDHB, failed to inhibit PDHA1 phosphorylation thereby inefficiently activating PDH. Heart tissue samples from carriers of the R2263Q exhibited lower PDH activity. Animal studies have revealed that homozygous $Notch1$ mutant mice die around days E9.5–E10.5, while mice lacking endothelial/endocardial $Notch1$ present with TOF-like characteristics. Although global $Notch1$ heterozygous mutant mice exhibit normal phenotype, with no obvious cardiovascular pathologies, $Notch1^{+/-}$, in a predominantly 129S6 background developed aortic root dilation[53], indicating the incomplete penetrance of $Notch1$ heterozygous mutants. In our study, we observed that the incidence of cardiac developmental defects in $Notch1^{+/-}$ embryos was not increased compared to wild-type embryos, but exposure to environmental stress, such as low-dose Hcy, increased the incidence of cardiac malformations in $Notch1^{+/-}$ embryos, while the wild-type offspring remained unaffected. Similar observations have been reported in studies of 22q11.2 deletion syndrome patients, where the duplication of the glucose transporter gene $SLC2A3A$ is associated with heart malformation phenotypes[54], indicating the importance of the interplay between genetic background and metabolic disorders in CHD pathogenesis. Furthermore, our study demonstrated that DCA supplementation during pregnancy protected $Notch1^{+/-}$ embryos exposed to Hcy from developing CHDs, suggesting a potential intervention strategy for preventing CHDs in individuals with certain genetic backgrounds. By integrating studies of TOF patients' tissue, functional validation of gene mutations, and in vivo investigations using mouse models, this study suggests that NOTCH1 mutations may contribute to the pathogenesis of CHD by inhibiting PDH activity. These findings indicate that mitochondrial metabolism could be a potential target for the early diagnosis and prevention of CHD. However, since this study reports only a single case of a TOF patient carrying NOTCH1 mutation with confirmed impaired PDH activity, additional patient cases and animal studies are required to substantiate and validate this proposed mechanism. Considering that only 30% of CHDs can be explained by genetic factors[55], while metabolic/nutrient factors, such as folate deficiency[56], gestational diabetes mellitus[57], obesity, alcohol intake, and high leucine level[58], have been reported to increase CHD risk,

Fig. 6 | NOTCH1 deficiency-induced pyruvate dehydrogenase (PDH) inactivation contributes to congenital heart defect (CHD) onset in mouse and human.
A Incidence of CHD in embryos of wild-type C57/Bl6 mice (WT), *Notch1*^{+/−} mice (KO), WT mice treated with low-dose homocysteine (Hcy) (0.5 g/L Hcy in drinking water orally administered to pregnant mice during E0.5 to E13.5) (WT+HCY), *Notch1*^{+/−} mice treated with Hcy (KO+HCY), WT mice treated with both Hcy and dichloroacetate (DCA) (10 mmol/L) (WT+HCY+DCA), and *Notch1*^{+/−} mice treated with both Hcy and DCA (KO+HCY+DCA). **B** PDH activity in mouse heart tissue isolated from WT, KO, WT+HCY, KO+HCY, WT+HCY+DCA, and KO+HCY+DCA mice (*n* = 5). **C** Schematic of NOTCH1 protein showing the location of 15 missense mutations identified in 300 tetralogy of Fallot (TOF) patients. EGF epidermal growth factor, LNR Lin-12/Notch repeats, HD-N N-terminus of heterodimerization, HD-C C-terminus of heterodimerization, TM transmembrane domain, RAM Rbp-associated molecule domain, ANKs ankyrin repeats, TAD transcription activation domain, PEST proline, glutamic acid, serine, threonine degradation domain, NLS nuclear localization signals. **D** Representative western blot illustrating the level of exogenously expressed wild-type NICD1 and NICD1 mutants G1814R, A2077P, R2263Q, V2285I, and I2456V, in cytoplasm or mitochondria of human umbilical vein endothelial cells (HUVEC). Cytochrome C oxidase subunit 4 (COX 4) and glyceraldehyde-3-phosphate dehydrogenase (GAPDH) were adopted as markers of mitochondria and cytoplasm fractions, respectively (*n* = 3). **E** Co-immunoprecipitation (CO-IP) of exogenous pyruvate dehydrogenase E1 subunit beta (PDHB) and G1814R, A2077P, R2263Q, V2285I, and I2456V mutants, in HUVEC (left) and human embryonic kidney 293T (HEK293T) (right) cells (*n* = 3).
F Representative western blot illustrating the phosphorylation level of pyruvate dehydrogenase E1 subunit alpha 1 (p-PDHA1) at serine 293 (Ser293), serine 232 (Ser232), and serine 300 (Ser300) in wild-type and *NOTCH1* knockout (*NOTCH1* KO) HEK293T cells (left) and in wild type and *NOTCH1* knockdown (*NOTCH1* KD) HUVEC (right) expressing exogenous wild-type NICD1 or NICD1 mutants (*n* = 3). **G** PDH activity detected in wild-type and *NOTCH1* KO HEK293T cells (left) and in wild-type and *NOTCH1* KD HUVEC (right) expressing exogenous wild-type NICD1 or NICD1 mutants (*n* = 5). **H** Relative PDH activity detected in heart tissue isolated from mouse and TOF patients carrying *NOTCH1* mutations or not (WT1, WT2, WT3, and WT4) (*n* = 3). For **B**, **D**, **E**, **G**, data are presented as mean values ± SD; *P* values were calculated by unpaired Student's *t* test with two-tailed analysis without adjustments.

future studies targeting metabolism hold promise for understanding CHD mechanisms and preventing the disease.

ECs lining the heart and blood vessel cavities exhibit special metabolic preferences, relying on glycolysis-derived ATP despite being immersed in oxygen-rich blood[14,59]. Although terminally differentiated, their final fates remain undecided. In the angiogenic environment, quiescent ECs shift to tip or stalk cells with elevated glycolysis rates to develop new vessels, while during embryogenesis or pathogenesis of

vascular diseases, they transition to mesenchymal cells to form valves and septum or to strengthen vessel walls. Metabolic alterations accompanying these transitions have long been viewed as consequences of cell fate; however, recent studies challenge this causal relationship. A recent study found that without additional known pro-angiogenic or anti-angiogenic factors, activating endothelial glycolysis alone via *PFKFB3* overexpression promotes EC shift to tip cells, whereas inhibiting glycolysis by knocking out *PFKFB3* or inhibiting fatty acid oxidation by silencing *CPT1* causes sprouting defects[15,60]. Correspondingly, impairing endothelial fatty acid metabolism by *Cpt2* knockdown induces EndMT[16]. Our data revealed that the classic pro-EndMT protein NOTCH1 activates mitochondrial respiration by directly activating mitochondrial PDH. Moreover, inhibiting PDH with PS-48 impedes the pro-EndMT effect of NOTCH1, while activating PDH with DCA induces significant EndMT, indicating that activating mitochondrial respiration triggers EC transition. Similarly, the role of metabolism in cell fate decisions in pluripotent cells[61] and immune cells[62] is being revaluated. A recent study revealed that cell fate transition is accompanied by shifts from canonical to non-canonical TCA cycle metabolism, wherein cytoplastic ACL regenerates oxaloacetate while bypassing canonical products such as αKG, succinate, and fumarate and blocks the non-canonical TCA cycle, thereby preventing cells from exiting pluripotency[63]. Further studies are warranted to determine whether alterations in the TCA cycle configuration accompany EC transitions and how metabolism influences cell fate determination.

The mitochondrial colocalization of NICD1 has been previously described in M1 macrophages and triple-negative breast cancer cells[28]. In M1 macrophages, NICD1 localizes to the mitochondrial displacement loop (D-loop) within the mitochondrial genome and upregulates the expression of several mtDNA-encoded components of the electron transport chain, including NADH dehydrogenase, cytochrome b, cytochrome c oxidase, and ATP synthases[26]. In glioma stem cells, NOTCH1 interacts with Rictor on the mitochondrial surface, activating the mTORC2/AKT pathway[49]. In ECs, NICD1 enters mitochondria and directly interacts with PDHB, leading to PDHA1 dephosphorylation and metabolic activation. Therefore, NICD1 plays a comprehensive role in regulating cell metabolism by (1) interacting with signaling pathways involved in metabolism regulation[48,50,64], (2) transcriptionally regulating both nuclear DNA- and mtDNA-encoded metabolic proteins[65], and (3) directly interacting with metabolic enzymes and activating enzymes. However, the collaboration between these mechanisms at different levels, especially regarding the intracellular distribution of NICD1, remains to be elucidated. We also attempted to unveil cellular signals regulating NICD1 entry into mitochondria. However, these attempts have not yield definitive results, despite various culture conditions tested, such as low oxygen, glucose starvation, and serum starvation (Supplementary Fig. 9). Therefore, further research is warranted to investigate regulatory factors around NICD entry into mitochondria. Besides, in this study, we primarily identified 427 potential interactors of NICD1 (Supplementary Data 1) and confirmed the interaction between NICD1 and PDHB. However, several proteins, including USP9X (ubiquitin-specific peptidase 9, X-linked), remain unverified. While USP9X has been reported to regulate Notch signaling[66] and was identified as a potential interactor, further experimental validation is needed to draw any definitive conclusion about its interaction with NICD1.

In conclusion, we present a mechanism by which NOTCH1 activates mitochondrial OXPHOS, showing that PDH activity is crucial for EndMT and therefore to normal heart development. Furthermore, we verified that the mutation c.6788 G > A (a.R2263Q) in *NOTCH1*, identified in TOF patients, impedes PDH regulation, implicating metabolism in TOF pathogenesis. Moreover, *Notch1*^{+/-} mice exhibited increased risks of having offspring with CHDs upon low-dose Hcy exposure, which was rescued by DCA supplementation during pregnancy,

suggesting a potential intervention strategy for CHD prevention with certain genetic backgrounds.

Methods

Study participants and ethics
Blood samples and heart tissue were collected from TOF patients at Children's Hospital of Fudan University between May 2017 and May 2022. The study design and conduct were approved and supervised by the Ethics Committee of Children's Hospital of Fudan University, according to the guidelines established by the Declaration of Helsinki. All experiments conformed to the Department of Health and Human Services Belmont Report. Written informed consent was obtained from all human participants. This research was conducted with the voluntary participation of individuals who were not offered any compensation. Sex or gender information was not collected, and no sex or gender analysis was carried out.

Animal use guidelines
All animal procedures were approved by the Institutional Animal Care and Use Committee of Fudan University and Anhui Medical University Institutional Animal Care and Use Committee. Methods employed were in accordance with the Guide for the Use and Care of Laboratory Animals.

Statistical analysis
Differences between the two groups were examined using the Student t-test. One-way ANOVA was used for three-group comparisons. A value of $P < 0.05$ was considered statistically significant. All data are expressed as mean ± SD. Prism version 8.0 and Microsoft Excel version 16.88 are used for data analysis.

Isolation of cardiac ECs and cardiomyocytes from rats and mice
Sprague-Dawley (SD) rats were obtained from the Anhui Medical University Experimental Animal Center, while *Notch1* heterozygous knockout (*Notch1*^{+/-}) mice and wild-type C57BL/6 J mice were purchased from GemPharmatech (Nanjing, China). 8–12-week animals were housed in a temperature- and humidity-controlled environment with a 12:12 h light: dark cycle. Animals were fed with normal chow for laboratory rodents (#1010010, Xietong, Jiangsu). The feeding schedule was maintained at regular intervals throughout the day. The amount of food consumed by each animal was monitored regularly to ensure proper nutrition and to detect any changes in eating behavior. Pregnant rats/mice were euthanized by cervical dislocation, and embryonic hearts were washed thrice in precooled phosphate-buffered saline (PBS), minced, and digested in an enzyme mixture (1:1 ratio of 0.25% trypsin to 0.1% collagenase). The resulting supernatant was centrifuged at $1000 \times g$ for 5 min at 4 °C, and cells were resuspended in Gey's solution (150 mM NH_4Cl and 10 mM $KHCO_3$) for 10 min on ice to lyse red blood cells. Following another centrifugation, cells were resuspended in 1 mL FACS staining buffer (PBS without Mg^{2+} or Ca^{2+} and with 1% FBS; pH 7.4) at a final concentration of 1×10^6 cells/50 μL and incubated with EC surface marker CD31 antibody (37-0700, Zymed, CA, USA) or myocardial cell marker cTnT (MA5-12960, Zymed) for 30 min. Cells were washed, resuspended in FACS staining buffer, and sorted using COULTER® EPICS® XLTM Flow Cytometer (Beckman Coulter, FL, USA).

Plasmid constructs
Detailed sequences of primers used are listed in the Supplementary Data 2. FLAG-tagged NICD1 (NICD1-FLAG) (pcDNA3.1), pyruvate dehydrogenase E1 subunit beta (PDHB)-HA (pcDNA3.1), and pRK7 (with cytochrome oxidase subunit 8 [COX8] presequence) plasmids were already developed in our laboratory. For eukaryotic expression plasmids, including the citrate synthase (CS)-FLAG (pcDNA3.1), the isocitrate dehydrogenase (NAD(+)) 3 non-catalytic subunit beta

(IDH3B) (pcDNA3.1), and stretches-deleted NICD1 (pcDNA3.1), CS (1401 bp) and IDH3B (1158 bp) were subcloned from the human cDNA library; NICD1-ΔM1 to NICD1-ΔM8 and truncated NICD1 were subcloned from NICD1-FLAG (pcDNA3.1). Phanta Max Super-Fidelity DNA Polymerase (Vazyme, Nanjing, China) was used for all. Then they were recombined with HA-tagged pcDNA3.1 or FLAG-tagged pcDNA3.1 vectors, linearized by EcoRI and XhoI (NEB, MA, USA), using ClonExpress-II One Step Cloning Kit (Vazyme). For plasmids designed for bimolecular fluorescence complementation (BiFC) assay, bFos (the 118–210 amino acids of Fos) and bJun (the 257–318 amino acids of Jun) were cloned from the human cDNA library; NICD1 and PDHB were cloned from existing plasmids, all recombined with linearized pBiFC-YN173 or pBiFC-YC155 (Yingrun Biotechnologies, Hunan, China). Point mutations were induced using Mut Express II Fast mutagenesis (Vazyme) according to manufacture's instruction, and the primers were also listed in the Supplementary Data 2.

Cell culture and transfection

Human umbilical vein endothelial cells (HUVEC) were obtained from ScienCell and were maintained in endothelial cell medium (ECM) (#1001, ScienCell, CA, USA) cultured on fibronectin (#8248, ScienCell)-coated cell culture plates. Cells were used between passages 3 and 5. Human embryonic kidney 293 T (HEK293T) cells, human gastric cancer cell line MKN45 and pancreatic cancer cell line BxPC-3, were cultured in Dulbecco's modified Eagle's medium (C11995500BT, Gibco, CA, USA) supplemented with 10% fetal bovine serum (Thermo Fisher Scientific, CA, USA), added 1% penicillin/streptomycin solution (10,000 U/mL and 10 mg/mL, respectively). Mycoplasma contamination was regularly checked. Cells cultured in six-well plates were transfected with 1 μg plasmids using 1.5 μL Lipofectamine 3000 and 2.0 μL p3000 (Life Technologies, CA, USA) at 70% confluence according to the manufacturer's instructions.

Knockout and knockdown of *NOTCH1*/*Notch1* in cell line and mouse

To knockout *NOTCH1* in the HEK293T cell line, CRISPR/Cas9 single-guide RNAs (sgRNAs) were designed using CHOPCHOP. Successful oligonucleotides are listed in Supplementary Data 2. Briefly, the oligos (produced by Tsingke, Beijing, China) were first phosphorylated and annealed (reaction mix: 1 μL 100 μM oligo 1, 1 μL 100 μM oligo 2, 1 μL 10× T4 Ligation Buffer [NEB], 6.5 μL ddH$_2$O, and 0.5 μL T4 Polynucleotide Kinase [NEB]), and then the oligo duplex was ligated to dephosphorylated Bbsl-digested pX459 vector (digesting reaction mix: 1 μg pX459 vector [Addgene], 1 μL FastDigest Bbsl [Thermo Fisher], 1 μL Fast AP [Thermo Fisher], 2 μL 10× FastDigest Buffer [Thermo Fisher], ddH$_2$O up to 20 μL in total; ligation reaction mix: 50 ng Bbsl-digested px459 vector, 1 μL phosphorylated and annealed oligo duplex [1:250 dilution], 1 μL 10× T4 Ligation Buffer, ddH$_2$O up to 10 μL subtotal, and 1 μL T4 Ligase [NEB]). Transfection and cell culture methods were performed as previously described. Puromycin (1 μg/mL) was added to normal culture media 48 h after transfection to identify successfully transfected cells. Knockout clones were identified by western blot analysis for the deficiency of NOTCH1 protein and sequencing of PCR products covering the target region with primers listed in Supplementary Data 2.

The *Notch1* knockout C57BL/6 J mouse was purchased from GemPharmatech. Briefly, sgRNA targeting exon2 of Notch1-201 (ENSMUST00000028288.4) transcript was transcribed in vitro. Cas9 and sgRNA were microinjected into fertilized eggs of C57BL/6 J mice. Fertilized eggs were transplanted to obtain positive F0 mice, confirmed by PCR and sequencing. A stable F1 generation mouse model was obtained by mating positive F0 generation mice with C57BL/6 J mice.

For knocking down *NOTCH1* in human cell lines and *Notch1* in mouse cell lines, small interfering RNA (siRNA) was used. Double-stranded human *NOTCH1* and mouse *Notch1* siRNAs were purchased from GenePharma (ShangHai, China) and transfected into cells using Lipo3000 (Invitrogen, CA, USA) according to the manufacturer's instructions. The sequences of siRNA targets used in this study are listed in Supplementary Data 2.

Subcellular fraction extraction

Subcellular fractions were extracted with differential centrifugation in STM buffer (250 mM sucrose, 50 mM Tris-HCl pH 7.4, 5 mM MgCl$_2$, protease, and phosphatase inhibitor cocktails) as described previously[30]. Tissue cells or scraped human umbilical vein endothelial cell (HUVEC) and HEK293T cells were washed with pre-cold PBS and pelleted by centrifugation at 200 × g for 7 min. All samples were resuspended in 300–500 μL of pre-cold STM buffer and homogenized for 1 min using a cold tissue lyser. The homogenate was kept on ice for 30 min, vortexed for 15 s, and centrifuged at 800 × g for 15 min to primarily isolate nuclei fractions. The resulting supernatant, containing mitochondrial and cytosolic fractions, was labeled as S, while the pellet containing nuclei and debris was labeled as NUC and was resuspended in 300–500 μL of STM buffer, vortexed for 15 s, and centrifuged at 500 × g for 15 min to purify the nuclear pellet. The S fraction, containing mitochondrial and cytosolic fractions, was centrifuged at 800 × g for 10 min to discard remaining nuclei fractions. The resulting supernatant was collected and centrifuged at 11,000 × g for 10 min. The resulting pellet was labeled as MITO, and the supernatant was labeled as CYTO. NUC and MITO fractions were resuspended in SDS-loading buffer; CYTO and LYS were supplemented with 20% 5 × SDS-loading buffer for further immunoblotting.

Immunofluorescence confocal microscopy

To determine the localization and expression of endogenous NOTCH1 and exogenous NICD1-FLAG in cells, HUVEC and HEK293T live cells cultured on poly-L-lysine-coated or fibronectin-coated glass-bottom cell culture dishes were labeled with 200 nM MitoTracker Red CMXRos (Invitrogen) for 30 min at 37 °C in fresh culture medium. After two washes with PBS, cells were fixed with 4% paraformaldehyde in PBS at 37 °C for 15 min, followed by two washes with PBS and permeabilization with 0.1% Triton X-100 in PBS for 5 min. Cells were blocked with 5% goat serum in PBS for 30 min and stained with rabbit polyclonal antibody against NOTCH1 (1:200, #4380, CST) or rabbit polyclonal antibody against FLAG (1:100) overnight. After washing with PBS, cells were incubated with Alexa 488-conjugated goat anti-rabbit antibody (A21206, Invitrogen) at 1:1,000 for 1 h. Cells were counterstained with DAPI for 5 min. Fluorescent optical images were captured using a Zeiss LSM880 confocal microscope and processed using ZEN software. To assess the expression of CD31 and α-SMA in EndMT assays, fixed and blocked HUVEC cells were stained with rabbit polyclonal antibody against α-SMA (1:200) and mouse monoclonal antibody against CD31 (1:200, #3528, Proteintech) overnight and incubated with Alexa 488-conjugated goat anti-rabbit antibody and Alexa 594-conjugated goat anti-mouse antibody (A11032, Invitrogen) at 1:1,000, following the abovementioned procedures.

Co-immunoprecipitation and pull-down assay

For screening NICD1-interacting proteins, HEK293T cells were transfected with pcDNA3.1-FLAG-NICD1(3 biological replicates) or vector (3 controls). NICD1-expressing and control cells were lysed on ice in 0.1% NP-40 buffer for 30 min and centrifuged to remove insoluble cell debris 48 h after transfection. The supernatant was filtered using 0.45-μM filters and incubated with FLAG-conjugated beads overnight at 4 °C. Precipitates were washed thrice with 0.1% NP-40 buffer, twice with ddH$_2$O, and thrice with 50 mmol/L NH$_4$CO$_3$ and subjected to tryptic digestion overnight at 37 °C. Peptides in the supernatant were collected by centrifugation, dried in a speed vacuum, and redissolved

in NH_4CO_3 buffer containing 0.1% formic acid and 5% acetonitrile for mass spectrometry analysis.

For co-immunoprecipitation (CO-IP) of exogenous proteins, HEK293T cells were transfected with eukaryotic expression plasmids and collected 36 h later. Cells were then lysed in cold 0.1% NP-40 buffer containing proteinase inhibitors; lysates were incubated with beads conjugated with anti-HA or anti-FLAG antibodies for 3 h at 4 °C. Beads were washed with 0.1% NP-40 buffer four times and boiled with 2× SDS-loading buffer for western blot assay. For CO-IP of endogenous NICD1 and PDH E1 subunit beta (PDHB), mouse heart tissue was lysed and incubated with rabbit anti-NOTCH1, anti-PDHB, or rabbit IgG as a negative control. Immunoprecipitation of endogenous PDH complex (PDC) components was performed using a PDH immunocapture kit (#ab109802, Abcam).

For the pull-down assay, GST-tagged PDHA1, PDHB, DLAT, DLD, and His-tagged NICD1 were constructed by inserting the coding regions of human PDHA1, PDHB, DLAT, DLD, and NICD1 into pGEX-6P-1 and pET-28a vectors. These recombinant plasmids were transformed into E. coli DH5α cells and induced with IPTG. Soluble lysates were prepared using protease and phosphatase inhibitors. GST-fusion proteins were purified using Glutathione Agarose (HY-K0211, MCE). His-NICD1 was purified using Ni-NTA His-Tag Purification Agarose (HY-K0210, MCE). His-NICD1 protein was incubated overnight with GST-fusion proteins or GST-control at 4 °C with shaking, followed by incubation with glutathione-sepharose beads for 2 h. Beads were washed thrice with binding buffer and boiled in SDS-loading buffer at 99 °C for 20 min. Western blot analysis was performed to detect bound proteins.

Protein extraction and tryptic digestion

The excised tissue-gel samples (6 samples, including 3 control and 3 pcDNA3.1-FLAG-NICD1 replicates) were washed in ddH2O three times at 25 °C and incubated with 50%/50% (v/v) acetonitrile (ACN)/ddH2O for 30 min at 30 °C on a shaker. The samples were then washed in 50%/50% (v/v) ACN/100 mM ammonium bicarbonate (ABB) for 10 min and dried in a SpeedVac at 45 °C for 3 min. The dried samples were treated with 20 mM TCEP for 30 min in darkness at 32 °C, followed by alkylation by the addition of 55 mM iodoacetamide (IAA) and incubation for 30 min in the dark at 25 °C. The sample pieces were further washed with 100 mM ABB. The samples were dehydrated by washing with 50%/50% (v/v) ACN/100 mM ABB 2 times for 5 minutes each at 25 °C on a shaker and then dried in a SpeedVac. Protein digestion was performed with 10 ng/μL trypsin in 25 mM ABB (pH = 8.0) by incubating twice at 37 °C for 4 h and 8 h. The digested peptide solutions were collected in the following steps and combined: 1) 30–40 μL of the supernatant was collected; 2) 100 μL of 25 mM ABB was added and vortexed for 10 min at 25 °C, and the supernatant was collected; 3) 100 μL of 50% ACN/2.5% formic acid was added, and the mixture was vortexed for 10 min; the supernatant was collected, and the process was repeated three times; and 4) 100 μL of 100% ACN was added, and the mixture was vortexed until the gel pieces turned white and sticky. Peptide samples were placed under vacuum to reduce the volume to 20–30 μL. The peptides were then desalted using C18 spin columns (Pierce™ C18 Spin Tips, Thermo Fisher Scientific, US) and dried in a SpeedVac. The cleaned peptides were stored at −20 °C until further analysis.

Nano-HPLC-MS/MS analysis

Peptides were resuspended in 10 μL solvent A (A: water with 0.1% formic acid; B: ACN with 0.1% formic acid) (3 biological replicates), separated by nanoLC, and analyzed using on-line electrospray tandem mass spectrometry. The experiments were conducted on an EASY-nLC 1000 system (Thermo Fisher Scientific, Waltham, MA) connected to an Orbitrap Fusion mass spectrometer (Thermo Fisher Scientific, San Jose, CA) with an online nano-electrospray ion source. A 3-μL peptide sample was loaded onto an analytical column (Acclaim PepMap C18,

75 μm × 25 cm) and separated using a linear gradient from 2% B to 30% B in 55 min. The column was re-equilibrated at initial conditions for 5 min. The column flow rate was maintained at 300 nL/min, and column temperature was maintained at 45 °C. An electrospray voltage of 2.3 kV versus the mass spectrometer inlet was used.

The Orbitrap Fusion mass spectrometer operated in data-dependent mode, switching automatically between MS and MS/MS acquisition. Survey full-scan MS spectra (m/z 350–1600) were acquired in the Orbitrap with a mass resolution of 60,000 at m/z 200. The AGC target was set to 1,000,000, and the maximum injection time was 50 ms. MS/MS acquisition was performed in the Orbitrap with a 3-s cycle time, a resolution of 15,000 at m/z 200, and an intensity threshold of 50,000. The maximum injection time was 65 ms. The AGC target was set to 100,000, and the isolation window was 1.6 m/z. Ions with charge states 2+, 3+, and 4+ were sequentially fragmented by higher energy collisional dissociation with a normalized collision energy of 30%. In all cases, one microscan was recorded using dynamic exclusion of 20 s. The MS/MS fixed first mass was set at 110.

Database search

Tandem mass spectra were extracted using Proteome Discoverer software (Thermo Fisher Scientific, version 1.4.0.288). Charge state deconvolution and deisotoping were not performed. All MS/MS samples were analyzed using Mascot (Matrix Science, London, UK; version 2.3.2). The Human UniProtKB/Swiss-Prot database (Release 2018-01-26, with 20,245 sequences) was used. Raw files from the Orbitrap Fusion were directly searched using a 10-ppm precursor mass tolerance and a 50-mmu fragment mass tolerance. Enzyme specificity with trypsin was applied. Up to two missed cleavages were allowed, and peptides with at least 7 amino acids were retained. Carbamidomethyl on cysteine was set as a fixed modification. Oxidation on methionine was set as a variable modification. Peptide-level false discovery rates were controlled to be <1% using the percolator algorithm.

BiFC assay

The BiFC assay was performed following previously described protocols with modifications[31]. Venus, an improved fluorescent protein, was used. Proteins were subcloned into the N-terminus or C-terminus of Venus individually. HEK293T cells underwent a series of transient transfections. Cells were stained with MitoTracker Red CMXRos and fixed with 4% paraformaldehyde 36 h after transfection. Fluorescence signals were observed using a Zeiss LSM880 confocal microscope.

Metabolite profiling

Cells were extracted using a tissue lyser (QIAGEN TissueLyser II, Germany) with 600 μL of precooled methanol-water mixture (2/1, v/v). Supernatant for each sample was collected after 10 min of centrifugation (11,180 × g, 4 °C). The extraction process was repeated twice. The three supernatants obtained for each sample were combined and centrifuged (16,099 × g, 4 °C) for 10 min. The resulting supernatants were lyophilized after removal of methanol in vacuo. The dried extracts were reconstituted into 600 μL of phosphate buffer (0.15 M, K_2HPO_4-NaH_2PO_4, pH 7.43) containing 80% D_2O (v/v) and trimethylsilyl propionate (TSP, 0.2915 mM). After centrifugation at 16,099 × g for 10 min at 4 °C, 550 μL of each supernatant was transferred into a standard 5-mm NMR tube for analysis.

One-dimensional ^1H NMR spectra were acquired at 298 K on a Bruker Advance III 600 MHz NMR spectrometer (600.13 MHz for proton frequency) equipped with a quaternary cryogenic inverse probe (Bruker Biospin, Germany) using the first increment of the gradient-selected NOESY pulse sequence (NOESYGPPR1D). Sixty-four transients were collected into 32 k data points with a spectral width of 20 ppm for each sample. The total relaxation delay time was 26 s, allowing for completely relaxed NMR spectra.

For resonance assignment, a series of 2D NMR spectra were acquired for selected samples and processed as previously reported[32,33]. These included 1H–1H correlation spectroscopy (COSY), 1H–1H total correlation spectroscopy (TOCSY), J-resolved spectroscopy (JRES), 1H–13 C heteronuclear single quantum correlation (HSQC), and 1H–13 C heteronuclear multiple bond correlation (HMBC) 2D NMR spectra.

Metabolite quantification

NMR spectra were processed using TOPSPIN software (V3.6.0, Bruker Biospin). For ^{1}H NMR spectra, an exponential window function was employed with a line broadening factor of 1 Hz and zero-filled to 128 k prior to Fourier transformation. Each spectrum was then phase- and baseline-corrected manually, with chemical shifts referenced to TSP (δ 0.00). Spectral regions were integrated into bins with a width of 0.002 ppm (1.2 Hz) using AMIX software (V3.8.3, Bruker Biospin). Absolute metabolite concentrations were calculated using the known TSP concentration.

In incompletely relaxed NMR spectra in our experiments, the integral area for a given proton resonance followed Eq. 1:

$$A^m = A_0^m \left[1 - \exp(-t/T_1^m) \right] \tag{1}$$

where t is total relaxation time (i.e., RD plus acquisition time); A_0^m and A^m are the integral areas for the signals of a given proton m (with spin-lattice relaxation time of T_1^m) in the completely relaxed state and a given spectrum, respectively. The relationship between the signal integrals for proton m and internal reference TSP in a given spectrum is described by Eq. 2:

$$\frac{A_0^m}{A_0^{TSP}} = \frac{A^m}{A^{TSP}} * \frac{1 - \exp(-t/T_1^{TSP})}{1 - \exp(-t/T_1^m)} \tag{2}$$

where A_0^{TSP} and A^{TSP} are the integrals for methyl groups of TSP in the completely relaxed state and a given spectrum, respectively; T_1^{TSP} is the spin-lattice relaxation time for methyl protons of TSP. The concentration of a metabolite (C_m) and TSP (C_{TSP}) in the same spectra is described by Eq. 3, accounting for proton numbers related to the NMR signals (Eq. 3):

$$C_m = \frac{N_{TSP} C_{TSP}}{N_m} * \frac{A_0^m}{A_0^{TSP}} = \frac{N_{TSP} C_{TSP}}{N_m} * \frac{A^m}{A^{TSP}} * \frac{1 - \exp(-t/T_1^{TSP})}{1 - \exp(-t/T_1^m)} \tag{3}$$

where N_m and N_{TSP} denote proton numbers for the corresponding metabolite signal and the methyl groups of TSP (i.e., 9 protons), respectively. This equation allows for the calculation of the concentration of a given metabolite using the known TSP concentration.

Metabolic flux assay

At 90% confluence, metabolic flux experiments were performed in HUVEC cells. After transfection for 48 h, cells were treated with 10 mM [U-^{13}C] glucose (Cambridge Isotope Labs, MA, USA) for 1 or 2 h before harvesting. After washing cells thrice with PBS, intracellular metabolites were extracted with using 1 mL pre-chilled 80% methanol. Supernatants were collected after centrifugation (12,000 × g, 4 °C) for 10 min. The extraction process was repeated twice, and supernatants were combined and lyophilized after vacuum drying to remove methanol. The resulting sample was resuspended in 1,500 μL of extraction solution (acetonitrile:methanol:water in 2:2:1 ratio, with isotopically labeled internal standard mixture). After 30 s of vortexing, samples were sonicated for 10 min in an ice-water bath. Next, samples were incubated for 1 h at −40 °C and centrifuged at 12,000 × g for 15 min at 4 °C. The resulting supernatant was transferred to a fresh glass vial for LC-MS/MS analysis.

LC-MS/MS analyses were performed using a UHPLC system (Vanquish, Thermo Fisher Scientific) with an UPLC BEH Amide column (2.1 × 100 mm, 1.7 μM) coupled to a Q Exactive HFX mass spectrometer (Orbitrap MS, Thermo Fisher Scientific). Abundances of ^{13}C-labeled metabolites were normalized relative to [U-^{13}C] glucose abundances in cells.

Mitochondrial respiratory function analysis

HEK293T (25,000 cells/well) or HUVEC (20,000 cells/well) cells were seeded in a 24-well XFe Cell Culture Microplate and incubated overnight ($n = 4$). Mitochondrial respiratory function was examined using Seahorse XFe 24 Extracellular Flux Analyzer (Agilent, CA, USA). A sensor cartridge was hydrated overnight. Reagents were loaded into the hydrated sensor cartridge ports as follows: Port A: 56 μL oligomycin (ATP synthase inhibitor) at 1.0 μM, Port B: 62 μL carbonyl cyanide-4 (trifluoromethoxy) phenylhydrazone (FCCP) (uncoupling agent) at 2.0 μM, Port C: 69 μL rotenone/antimycin A (rotenone, mitochondrial complex-I inhibitor; antimycin A, mitochondrial complex-III inhibitor) at 0.5 μM. Cell culture media were replaced with FBS-free medium containing XF Base Medium supplemented with 10 mM glucose, 1 mM pyruvate, and 2 mM glutamine (Agilent). After sensor cartridge calibration, the XF Cell-Culture Microplate was inserted into the instrument for three measurement cycles. All data were normalized by protein content and analyzed using Wave software.

EndMT assays

For cytokine-induced EndMT, HUVEC were seeded on fibronectin-coated plates at 10,000 cells/cm^2 in complete ECM containing 1% EC growth supplement (ECGS) and 5% FBS. After 24 h, the medium was replaced with fresh EndMT-ECM containing 1% ECGS and 0.2% FBS, supplemented with 10 ng/mL TGF-β1 (100-21-10, Peprotech, NJ, USA) and 1 ng/mL IL-1β (200-01B, Peprotech). For transfection-induced EndMT, subconfluent HUVEC on fibronectin-coated 6-well plates were cultured in complete ECM and transfected. Complete ECM was replaced with fresh EndMT-ECM 24–36 h after transfection. For chemically induced EndMT, subconfluent HUVEC (transfected or not) in fresh EndMT-ECM were incubated with the PDH inhibitor, PS-48 (Santa Cruz Biotechnology, CAS1180676-32-7) at a final concentration of 100 μmol/L, or with the PDH-activator DCA (Sigma-Aldrich, 347795) at a final concentration of 5–20 mmol/L. EndMT was evaluated by measuring the expression of endothelial (CD31, VE-cadherin, VEGF receptor) and EndMT markers (α-SMA, Vimentin, N-cadherin) via immunofluorescence microscopy or western blot 7 days post-treatment.

ATP and PDH, CS, IDH activity measurements

To measure ATP, cells cultured in opaque 96-well plates were resuspended with 100 μL medium and equilibrated to room temperature. Subsequently, 100 μL of CellTiter-Glo 2.0 (Promega, WI, USA) reagent was added to the suspension and mixed for 2 min on an orbital shaker. After 10-min incubation at room temperature, the relative luciferase units were measured by SpectraMax i3x (Molecular Devices, CA, USA). To measure PDH, CS, and IDH activity of cells, harvested cells were washed twice in PBS, and subjected to PDH-Enzyme-Activity Microplate Assay (ab109902, Abcam), a CS activity kit (K287-100, Biovision), and a IDH kit (ab102528, Abcam) according to manufacturer's instructions.

Western blotting

Briefly, protein samples were boiled in sodium dodecyl sulfate (SDS)-loading buffer. The samples were separated in SDS-PAGE gel (8%–12%) and transferred to nitrocellulose membranes. After blocking with 5% skim milk, membranes were incubated with specific primary antibodies, including NOTCH1 (1:1000, #3608, CST, MA, USA), Histone H3

(H3) (1:5000, P30266, abmart, Shanghai, China), GAPDH (1:5000, 30201ES20, Yeasen, Shanghai, China), COX4 (1:3000, #4850, CST), FLAG (1:5,000, M20008, abmart), HA (1:5,000, M20021, abmart), CS (1:1,000, EPR8067, Abcam), ACTIN (1:5000, 30102ES40, Yeasen), pyruvate dehydrogenase E1 subunit alpha (PDHA1) (1:1,000, #3205, CST), PDHB (1:1000, 14744-1-AP, Proteintech, IL, USA), dihydrolipoyl dehydrogenase (DLD) (1:1000, 16431-1-AP, Proteintech), dihy-drolipoamide S-acetyltransferase (DLAT) (1:1000, #12362, CST), pyruvate dehydrogenase kinase (PDK) 1 (PDK1) (1:1000, #3820, CST), PDK2 (1:1000, 15647-1-AP, Proteintech), PDK3 (1:1000, 12215-1-AP, Proteintech), PDK4 (1:1000, 12949-1-AP, Proteintech), p-PDHA (1:500, S293) (ab177461, Abcam), p-PDHA (S232) (1:500, 29582-1-AP, Pro-teintech), p-PDHA (S300) (1:500, 80572-1-RR, Proteintech), CD31 (1:1000, #3528, CST), VE-Cadherin (1:1000, VE-Cad, #3528, CST), vas-cular endothelial growth factor receptor (VEGFR) (1:1000, #2893, CST), α smooth muscle actin (1:1000,α-SMA) (14395-1-AP, Pro-teintech), N-Cadherin (1:500, N-Cad, #4061, CST), and Vimentin (1:500, 10366-1-AP, Proteintech), overnight at 4 °C. After washing, membranes were incubated with the corresponding secondary anti-bodies for 1 h at room temperature. The blots were visualized with Pierce ECL Plus (32132#, Thermo Fisher Scientific). Images were pro-cessed and quantified using Image J software (National Institutes of Health, MD, USA).

Quantitative real-time reverse transcription (qRT)-PCR
RNA from cultured cells was prepared with TransZol (Trans Gen Bio-tech Co. Ltd.) and cDNA was synthesized from 5 µg RNA with Trans-Script First-Strand cDNA synthesis Super Mix (Trans Gen Biotech Co. Ltd.). Gene expression was determined by real-time PCR using the iQTM SYBR Green SuperMix Kit (BIO-RAD) on an CFX96TM Real-Time system (BIO-RAD). All data were normalized to ACTB expression. All primer sequences are listed in Supplementary Data 2.

NOTCH1 mutation identification and heart tissue collection from TOF patients
Blood samples were collected from TOF patients diagnosed by cardi-ologists at Children's Hospital of Fudan University with written con-sent. Blood samples (3–5 mL) were collected in EDTA anticoagulant tubes and stored at −20 °C. DNA was extracted using conventional extraction methods and sequenced by Sanger sequencing. Primers for sequencing *NOTCH1* exons are listed in Supplementary Data 2. Heart tissue from TOF patients was collected as remnants during cardiac surgery at the Children's Hospital of Fudan University.

Reporting summary
Further information on research design is available in the Nature Portfolio Reporting Summary linked to this article.

Data availability
The mass spectrometry proteomics data have been deposited to the ProteomeXchange Consortium via the PRIDE[67] partner repository with the dataset identifier PXD054146. All other data are available in the article and its Supplementary files. Source data are provided with this paper.

References
1. McKellar, S. H. et al. Novel NOTCH1 mutations in patients with bicuspid aortic valve disease and thoracic aortic aneurysms. *J. Thorac. Cardiovasc Surg.* **134**, 290–296 (2007).
2. Garg, V. et al. Mutations in NOTCH1 cause aortic valve disease. *Nature* **437**, 270–274 (2005).
3. Page, D. J. et al. Whole exome sequencing reveals the major genetic contributors to nonsyndromic tetralogy of fallot. *Circ. Res.* **124**, 553–563 (2019).
4. Andersson, E. R., Sandberg, R. & Lendahl, U. Notch signaling: sim-plicity in design, versatility in function. *Development* **138**, 3593–3612 (2011).
5. D'Amato, G. et al. Sequential Notch activation regulates ventricular chamber development. *Nat. Cell Biol.* **18**, 7–20 (2016).
6. Del Monte, G., Grego-Bessa, J., Gonzalez-Rajal, A., Bolos, V. & De La Pompa, J. L. Monitoring Notch1 activity in development: evidence for a feedback regulatory loop. *Dev. Dyn.* **236**, 2594–2614 (2007).
7. Piera-Velazquez, S. & Jimenez, S. A. Endothelial to mesenchymal transition: role in physiology and in the pathogenesis of human diseases. *Physiol. Rev.* **99**, 1281–1324 (2019).
8. Kovacic, J. C., Mercader, N., Torres, M., Boehm, M. & Fuster, V. Epithelial-to-mesenchymal and endothelial-to-mesenchymal tran-sition: from cardiovascular development to disease. *Circulation* **125**, 1795–1808 (2012).
9. Hofmann, J. J. et al. Endothelial deletion of murine Jag1 leads to valve calcification and congenital heart defects associated with Alagille syndrome. *Development* **139**, 4449–4460 (2012).
10. Pierpont, M. E., Markwald, R. R. & Lin, A. E. Genetic aspects of atrioventricular septal defects. *Am. J. Med. Genet.* **97**, 289–296 (2000).
11. Maleki, S. et al. Endothelial/epithelial mesenchymal transition in ascending aortas of patients with bicuspid aortic valve. *Front. Car-diovasc. Med.* **6**, 182 (2019).
12. Li, Y., Lui, K. O. & Zhou, B. Reassessing endothelial-to-mesenchymal transition in cardiovascular diseases. *Nat. Rev. Cardiol.* **15**, 445–456 (2018).
13. Rohlenova, K., Veys, K., Miranda-Santos, I., De Bock, K. & Carmeliet, P. Endothelial cell metabolism in health and disease. *Trends Cell Biol.* **28**, 224–236 (2018).
14. Li, X., Sun, X. & Carmeliet, P. Hallmarks of endothelial cell meta-bolism in health and disease. *Cell Metab.* **30**, 414–433 (2019).
15. De Bock, K. et al. Role of PFKFB3-driven glycolysis in vessel sprouting. *Cell* **154**, 651–663 (2013).
16. Xiong, J. et al. A metabolic basis for endothelial-to-mesenchymal transition. *Mol. Cell* **69**, 689–698.e687 (2018).
17. Noseda, M. et al. Notch activation results in phenotypic and func-tional changes consistent with endothelial-to-mesenchymal trans-formation. *Circ. Res.* **94**, 910–917 (2004).
18. Timmerman, L. A. et al. Notch promotes epithelial-mesenchymal transition during cardiac development and oncogenic transforma-tion. *Genes Dev.* **18**, 99–115 (2004).
19. Liu, J., Dong, F., Jeong, J., Masuda, T. & Lobe, C. G. Constitutively active Notch1 signaling promotes endothelial-mesenchymal tran-sition in a conditional transgenic mouse model. *Int. J. Mol. Med.* **34**, 669–676 (2014).
20. Niessen, K. et al. Slug is a direct Notch target required for initiation of cardiac cushion cellularization. *J. Cell Biol.* **182**, 315–325 (2008).
21. Niessen, K. & Karsan, A. Notch signaling in cardiac development. *Circ. Res.* **102**, 1169–1181 (2008).
22. Garside, V. C., Chang, A. C., Karsan, A. & Hoodless, P. A. Co-ordinating Notch, BMP, and TGF-beta signaling during heart valve development. *Cell Mol. Life Sci.* **70**, 2899–2917 (2013).
23. Fre, S. et al. Notch signals control the fate of immature progenitor cells in the intestine. *Nature* **435**, 964–968 (2005).
24. Gao, F. et al. Notch pathway is involved in high glucose-induced apoptosis in podocytes via Bcl-2 and p53 pathways. *J. Cell Biochem.* **114**, 1029–1038 (2013).
25. Briot, A. et al. Endothelial NOTCH1 is suppressed by circulating lipids and antagonizes inflammation during atherosclerosis. *J. Exp. Med.* **212**, 2147–2163 (2015).
26. Xu, J. et al. NOTCH reprograms mitochondrial metabolism for proinflammatory macrophage activation. *J. Clin. Invest.* **125**, 1579–1590 (2015).

27. Jabs, M. et al. Inhibition of endothelial notch signaling impairs fatty acid transport and leads to metabolic and vascular remodeling of the adult heart. *Circulation* **137**, 2592–2608 (2018).

28. Hossain, F. et al. Notch signaling regulates mitochondrial metabolism and nf-kappab activity in triple-negative breast cancer cells via IKKalpha-dependent non-canonical pathways. *Front. Oncol.* **8**, 575 (2018).

29. Basu, M. et al. Epigenetic mechanisms underlying maternal diabetes-associated risk of congenital heart disease. *JCI Insight* **2**, e95085 (2017).

30. Savolainen, S. M., Foley, J. F. & Elmore, S. A. Histology atlas of the developing mouse heart with emphasis on E11.5 to E18.5. *Toxicol. Pathol.* **37**, 395–414 (2009).

31. Savojardo, C., Bruciaferri, N., Tartari, G., Martelli, P. L. & Casadio, R. DeepMito: accurate prediction of protein sub-mitochondrial localization using convolutional neural networks. *Bioinformatics* **36**, 56–64 (2020).

32. Bolender, N., Sickmann, A., Wagner, R., Meisinger, C. & Pfanner, N. Multiple pathways for sorting mitochondrial precursor proteins. *EMBO Rep.* **9**, 42–49 (2008).

33. Claros, M. G. & Vincens, P. Computational method to predict mitochondrially imported proteins and their targeting sequences. *Eur. J. Biochem.* **241**, 779–786 (1996).

34. Fukasawa, Y. et al. MitoFates: improved prediction of mitochondrial targeting sequences and their cleavage sites. *Mol. Cell Proteom.* **14**, 1113–1126 (2015).

35. Wang, W. et al. The inhibition of TDP-43 mitochondrial localization blocks its neuronal toxicity. *Nat. Med.* **22**, 869–878 (2016).

36. Schmidt, O., Pfanner, N. & Meisinger, C. Mitochondrial protein import: from proteomics to functional mechanisms. *Nat. Rev. Mol. Cell Biol.* **11**, 655–667 (2010).

37. Ciszak, E. M., Korotchkina, L. G., Dominiak, P. M., Sidhu, S. & Patel, M. S. Structural basis for flip-flop action of thiamin pyrophosphate-dependent enzymes revealed by human pyruvate dehydrogenase. *J. Biol. Chem.* **278**, 21240–21246 (2003).

38. Kim, J. W., Tchernyshyov, I., Semenza, G. L. & Dang, C. V. HIF-1-mediated expression of pyruvate dehydrogenase kinase: a metabolic switch required for cellular adaptation to hypoxia. *Cell Metab.* **3**, 177–185 (2006).

39. Saunier, E., Benelli, C. & Bortoli, S. The pyruvate dehydrogenase complex in cancer: an old metabolic gatekeeper regulated by new pathways and pharmacological agents. *Int J. Cancer* **138**, 809–817 (2016).

40. Stacpoole, P. W. Therapeutic targeting of the pyruvate dehydrogenase complex/pyruvate dehydrogenase kinase (PDC/PDK) axis in cancer. *J. Natl Cancer Inst.* **109**, djx071 (2017).

41. Patel, M. S. & Korotchkina, L. G. Regulation of the pyruvate dehydrogenase complex. *Biochem Soc. Trans.* **34**, 217–222 (2006).

42. Sutendra, G. et al. A nuclear pyruvate dehydrogenase complex is important for the generation of acetyl-CoA and histone acetylation. *Cell* **158**, 84–97 (2014).

43. Holness, M. J. & Sugden, M. C. Regulation of pyruvate dehydrogenase complex activity by reversible phosphorylation. *Biochem. Soc. Trans.* **31**, 1143–1151 (2003).

44. Rieder, F. et al. Inflammation-induced endothelial-to-mesenchymal transition: a novel mechanism of intestinal fibrosis. *Am. J. Pathol.* **179**, 2660–2673 (2011).

45. Siebel, C. & Lendahl, U. Notch signaling in development, tissue homeostasis, and disease. *Physiol. Rev.* **97**, 1235–1294 (2017).

46. Landor, S. K. et al. Hypo- and hyperactivated Notch signaling induce a glycolytic switch through distinct mechanisms. *Proc. Natl Acad. Sci. USA* **108**, 18814–18819 (2011).

47. Lee, S. Y. & Long, F. Notch signaling suppresses glucose metabolism in mesenchymal progenitors to restrict osteoblast differentiation. *J. Clin. Invest.* **128**, 5573–5586 (2018).

48. Zheng, X. et al. Interaction with factor inhibiting HIF-1 defines an additional mode of cross-coupling between the Notch and hypoxia signaling pathways. *Proc. Natl Acad. Sci. USA* **105**, 3368–3373 (2008).

49. Lee, K. S. et al. Roles of PINK1, mTORC2, and mitochondria in preserving brain tumor-forming stem cells in a noncanonical Notch signaling pathway. *Genes Dev.* **27**, 2642–2647 (2013).

50. Vilimas, T. et al. Targeting the NF-kappaB signaling pathway in Notch1-induced T-cell leukemia. *Nat. Med.* **13**, 70–77 (2007).

51. Margalef, P. et al. A truncated form of IKKalpha is responsible for specific nuclear IKK activity in colorectal cancer. *Cell Rep.* **2**, 840–854 (2012).

52. Bhola, N. E. et al. Treatment of triple-negative breast cancer with TORC1/2 Inhibitors sustains a drug-resistant and notch-dependent cancer stem cell population. *Cancer Res.* **76**, 440–452 (2016).

53. Koenig, S. N. et al. Notch1 haploinsufficiency causes ascending aortic aneurysms in mice. *JCI Insight* **2**, e91353 (2017).

54. Mlynarski, E. E. et al. Copy-number variation of the glucose transporter gene SLC2A3 and congenital heart defects in the 22q11.2 deletion syndrome. *Am. J. Hum. Genet.* **96**, 753–764 (2015).

55. Russell, M. W., Chung, W. K., Kaltman, J. R. & Miller, T. A. Advances in the understanding of the genetic determinants of congenital heart disease and their impact on clinical outcomes. *J. Am. Heart Assoc.* **7**, e006906 (2018).

56. Wang, D. et al. Lower circulating folate induced by a fidgetin intronic variant is associated with reduced congenital heart disease susceptibility. *Circulation* **135**, 1733–1748 (2017).

57. Oyen, N. et al. Prepregnancy diabetes and offspring risk of congenital heart disease: a Nationwide Cohort Study. *Circulation* **133**, 2243–2253 (2016).

58. Zhang, X. et al. Gestational leucylation suppresses embryonic t-box transcription factor 5 signal and causes congenital heart disease. *Adv. Sci. (Weinh.).* **9**, e2201034 (2022).

59. Fitzgerald, G., Soro-Arnaiz, I. & De Bock, K. The warburg effect in endothelial cells and its potential as an anti-angiogenic target in cancer. *Front. Cell Dev. Biol.* **6**, 100 (2018).

60. Schoors, S. et al. Fatty acid carbon is essential for dNTP synthesis in endothelial cells. *Nature* **520**, 192–197 (2015).

61. Mosteiro, L., Hariri, H. & van den Ameele, J. Metabolic decisions in development and disease. *Development* **148**, dev199609 (2021).

62. Ohradanova-Repic, A., Boes, M. & Stockinger, H. Editorial: role of metabolism in regulating immune cell fate decisions. *Front. Immunol.* **11**, 527 (2020).

63. Arnold, P. K. et al. A non-canonical tricarboxylic acid cycle underlies cellular identity. *Nature* **603**, 477–481 (2022).

64. Graziani, I. et al. Opposite effects of Notch-1 and Notch-2 on mesothelioma cell survival under hypoxia are exerted through the Akt pathway. *Cancer Res.* **68**, 9678–9685 (2008).

65. Basak, N. P., Roy, A. & Banerjee, S. Alteration of mitochondrial proteome due to activation of Notch1 signaling pathway. *J. Biol. Chem.* **289**, 7320–7334 (2014).

66. Jaiswal, A. et al. Therapeutic inhibition of USP9x-mediated Notch signaling in triple-negative breast cancer. *Proc. Natl Acad. Sci. USA* **118**, e2101592118 (2021).

67. Perez-Riverol, Y. et al. The PRIDE database resources in 2022: a hub for mass spectrometry-based proteomics evidences. *Nucleic Acids Res.* **50**, D543–D552 (2022).

Acknowledgements

Author contributions

Competing interests

The authors declare no competing interests.

Additional information

Supplementary information The online version contains supplementary material available at https://doi.org/10.1038/s41467-024-54407-7.

Correspondence and requests for materials should be addressed to Feng Wang, Yong-Hao Gui, Hui Tao or Jian-Yuan Zhao.

Peer review information *Nature Communications* thanks Jason Kovacic, Michael Simons and the other, anonymous, reviewer(s) for their contribution to the peer review of this work. A peer review file is available.

Reprints and permissions information is available at http://www.nature.com/reprints

Publisher's note Springer Nature remains neutral with regard to jurisdictional claims in published maps and institutional affiliations.